International Journal of Multiphase Flow 171 (2024) 104661

Contents lists available at ScienceDirect

International Journal of Multiphase Flow

journal homepage: www.elsevier.com/locate/ijmulflow

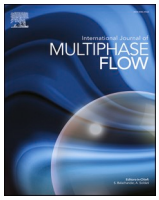

Extension of the delayed equilibrium model to flashing flows of organic fluids in converging-diverging nozzles

Carlotta Tammone [a,*], Alessandro Romei [b], Giacomo Persico [b], Fredrik Haglind [a]

[a] Department of Civil and Mechanical Engineering, Technical University of Denmark, Koppels Allé, 2800 Kongens Lyngby, Denmark
[b] Laboratory of Fluid Machines, Energy Department, Politecnico di Milano, Via Lambruschini 4, 20156 Milano, Italy

ARTICLE INFO

Keywords:
Two-phase flow
Flashing flow
Organic fluid
Non-equilibrium
Delayed equilibrium model
Nozzle

ABSTRACT

Flashing flows of organic fluids find application in various energy systems, but the available modelling approaches rely on semi-empirical correlations calibrated for other fluids and operating conditions. This paper extends the state-of-the-art one-dimensional models developed for water to flashing of organic fluids, using R134a as a reference. First, the delayed equilibrium model combined with Grönnerud's friction correlation is identified as the most appropriate approach, reducing the error on mass flow rate with respect to experimental results from 48.3 %, obtained with the homogeneous equilibrium model, to 10.3 %. Then, the traditionally adopted incompressible flow assumption for the metastable liquid phase is replaced by a dedicated thermodynamic model, preventing the appearance of unphysical metastable phase temperatures. Moreover, the delayed equilibrium model is tailored to R134a by tuning the semi-empirical coefficients of the constitutive law. The proposed modifications to the state-of-the-art delayed equilibrium model result in an improvement in the prediction of the pressure profiles and the mass flow rate for flashing flows of R134a, with a decrease in the error on mass flow rate from 10.3 % to 6.1 % with respect to the original formulation.

1. Introduction

Two-phase flows characterized by flashing or cavitation are frequently encountered in energy systems. The phenomenon of flashing consists of the nucleation of vapour bubbles in a liquid flow that undergoes a fast depressurization and reaches saturation conditions. If the expansion below saturation occurs locally, the nucleated vapour bubbles implode when travelling through high-pressure regions, generating the cavitation phenomenon. In supercritical CO_2 power systems, cavitation can occur in the compressor as the fluid close to critical conditions accelerates at the leading edge of the impeller, causing a local reduction of pressure (Lettieri et al., 2015; Persico et al., 2021); similar cavitation phenomena may occur in pumps, when the intake thermodynamic state is close to saturation. In ejector-based heat pumps (Rony et al., 2019) and refrigeration systems (Lee et al., 2011; Sumeru et al., 2012) flashing occurs in the motive nozzle of the ejector, where the nearly-saturated liquid vaporizes while accelerating to supersonic conditions. Furthermore, two-phase flashing of organic fluids occurs in volumetric expanders (Smith and da Silva, 1994; van Heule et al., 2023) and turbo-expanders (Tammone et al., 2021; White, 2021) used in power generation systems based on trilateral and partial evaporation cycles, and in throttling valves for refrigeration and cryogenic liquefaction systems (Simões-Moreira and Bullard, 2003). In order to improve the performance and extend the life of the components where the flashing phenomenon takes place, it is crucial to predict accurately the onset of vapour nucleation and the evolution of the flow, avoiding the occurrence of local bubble implosion or fully exploiting the two-phase expansion.

Flashing flows are characterized by a simultaneous depressurization and acceleration of the flow in ducts with variable cross-section. As soon as bubble nucleation occurs, the compressibility of the fluid is increased significantly (Lund and Flåtten, 2010; Nguyen et al., 1981) and the coupling between pressure and density fields becomes stronger. The compressibility and, consequently, the evolution of the flow during flashing are affected by the rate of vaporization and by the onset of thermodynamic non-equilibrium phenomena, which are in turn determined by the local flow conditions. The difficulties in predicting the vapour nucleation process, the distribution of the phases and their interaction, and ultimately the thermodynamic properties of the mixture make the modelling of two-phase flashing flows challenging. Despite the significant research effort, a thorough understanding of the flashing phenomenon is still lacking and a comprehensive theory has not yet been proposed (Liao and Lucas, 2021, 2017; Pinhasi et al., 2005).

* Corresponding author.
E-mail address: carta@dtu.dk (C. Tammone).

https://doi.org/10.1016/j.ijmultiphaseflow.2023.104661
Received 6 July 2023; Received in revised form 22 October 2023; Accepted 30 October 2023
Available online 2 November 2023

Nomenclature

Latin symbols

A	area
c	specific heat capacity
C	constant, friction factor
d	grid refinement parameter
D	diameter
e	global solution residual
G	mass flux
h	specific enthalpy
k	thermal conductivity, roughness, constant
L	length
$\dot{m}$	mass flow rate
P	pressure, perimeter
p	pressure
R	radius
s	specific entropy
T	temperature
v	velocity
x	vapour quality
y	void fraction
z	position along the nozzle axis

Greek symbols

β	Pressure ratio
Δ	Difference, gradient
δ	Boundary layer thickness, choking margin
γ	Mass fraction of mixture in equilibrium
μ	Dynamic viscosity
ν	Specific volume
Φ	Parameter
ψ, ϕ	Generic variable
ρ	Density
τ	Shear stress
ϑ	Opening angle of the nozzle
ε	Volume fraction

Subscripts

0	total
B	bubble
c	calculated
cr	critical
d	desired
exp	experimental
i	i-th section, i-th values
in	inlet
L	liquid
LM	Lockhart-Martinelli
LV	difference between vapour and liquid
m	metastable
min	minimum
nuc	nucleation
out	outlet
R	relative
$RMSR$	root mean square relative
sat	saturation
T	thermal
th	throat
V	vapour
w	wall
z	at location z

Abbreviations

CFD	Computational Fluid Dynamics
DEM	Delayed Equilibrium Model
EoS	Equation of state
HEM	Homogeneous Equilibrium Model
HEOS	Helmholtz energy Equation Of State

In technical applications of flashing flows, such as ejector motive nozzles, valves and expanders, the main issues associated to the bubble nucleation concern the prediction of the choked, or critical, mass flow rate, i.e. the maximum mass flow rate that the device is able to convey, and the corresponding pressure levels. Currently, the prediction of flows under flashing expansion still relies mostly on the adoption of empirical correlations that model the vaporization process while considering the two-phase fluid as constituted by two continuous and interacting phases, according to the so-called Eulerian-Eulerian approach (Brennen, 2005; Ishii and Hibiki, 2006; Liao and Lucas, 2017; Ringstad et al., 2020). Within the Eulerian-Eulerian approach, mixture models are characterized by the formulation of transport equations of mass, momentum and energy for the two-phase mixture characterized by average properties. Mixture models require just a constitutive law for the vaporization rate and possibly for the velocity ratio, or slip, between the phases. Since these quantities can be more easily derived from void fraction, temperature and pressure measurements, mixture models have been traditionally preferred when a limited amount of experimental data on the fluid is available. An example is CO_2, for which mixture models have been mainly used, both through one-dimensional in-house models (Angielczyk et al., 2020, 2019) and through commercial CFD software (Giacomelli et al., 2018; Romei and Persico, 2021).

Due to the quasi one-dimensional flow configuration, converging-diverging nozzles have been traditionally used to investigate expanding flows experimentally and numerically and to develop appropriate thermodynamic and fluid-dynamic models. Flashing flows of water in converging-diverging nozzles for a wide range of operating conditions were successfully modelled through one-dimensional mixture models (Bartosiewicz and Seynhaeve, 2013; De Lorenzo et al., 2017; Downar-Zapolski et al., 1996). As thermodynamic non-equilibrium effects were found to be significant for flashing water, two approaches were proposed, which relax the thermodynamic equilibrium assumption. In the homogeneous relaxation model (HRM) a relaxation law accounts for the finite vaporization rate (Bilicki and Kestin, 1990; Downar-Zapolski et al., 1996), whereas for the delayed equilibrium model (DEM), the mass fraction of the mixture evolving in non-equilibrium conditions is correlated to the local flow conditions (Bartosiewicz and Seynhaeve, 2013; De Lorenzo et al., 2017; Feburie et al., 1993). On the contrary, experimental (Nakagawa et al., 2009) and numerical (Angielczyk et al., 2020, 2019, 2010; Romei and Persico, 2021) investigation of flashing flows of CO_2 near the critical point suggested that flashing occurs, in very good approximation, according to homogeneous and equilibrium conditions. For such applications, the homogeneous equilibrium model (HEM) can therefore be adopted (Palacz et al., 2015; Romei and Persico, 2021). However, multiple formulations of the DEM for CO_2 have been proposed (Angielczyk et al., 2020, 2019) in order to match more closely the experimental data, but the difference in the results between the HEM and the DEM developed for CO_2 was found to be smaller than that observed when adopting different friction loss correlations. However, for flashing flows of CO_2 far from the critical point, the adoption of the DEM is expected to give more accurate results than the HEM, though this cannot be verified due to the lack of experimental data in the open literature. One of the main open issues of the DEM is the thermodynamic modelling of the metastable phase, which has been assumed

incompressible by all authors so far (Angielczyk et al., 2020; De Lorenzo et al., 2017). Despite being realistic at low reduced pressures, typical of water applications, this assumption affects significantly the prediction of the thermodynamic properties of the metastable liquid phase at higher reduced pressures.

Despite their relevance for promising applications, flashing flows of organic fluids have been investigated to a very limited extent, probably because of the lack of experimental data. Just recently an experimental study on flashing flows of R134a in converging-diverging nozzles was published (Zhu and Elbel, 2019) and the measurements were compared with numerical results from a two-fluid CFD model (Zhu and Elbel, 2020). A good agreement between CFD results and experimental data was found in terms of pressure distribution and mass flow rate, but a strong stratification of the flow was also predicted, which was not confirmed by the visualization of the flow. A study conducted on the same set of experimental data with a 1D mixture model adopting thermodynamic equilibrium (Tammone et al., 2023) suggested that strong non-equilibrium phenomena are present and emphasized the need for dedicated models. To the best of the authors' knowledge, the only analysis of flashing of organic fluids documented so far is the one proposed by White (2022), who applied a one-dimensional two-fluid model to the two-phase expansion of R1233zd(E) and MM; however, the numerical results were not validated with experimental data.

Further research work on the flashing of organic fluids is crucial because the typical operating conditions are different from those of water and CO_2 flows and because fluid-dependent transport and thermodynamic properties are expected to have a significant impact on mass and heat transfer phenomena and on viscous losses. This paper aims at extending the state-of-the-art one-dimensional delayed equilibrium model developed for water to flashing of organic fluids. Throughout the work, R134a is adopted as reference organic fluid, since it is the only organic fluid for which experimental data are currently available. In order to assess its suitability for flashing of organic fluids, the original one-dimensional DEM developed for water is applied to the flashing of R134a and the results are compared to experimental data. Since flashing flows in small devices are strongly influenced by viscous losses, several friction loss correlations are tested to identify the most suitable one for R134a. Moreover, an improvement to the original DEM is proposed by replacing the commonly employed incompressible flow assumption with a different approach to model the thermodynamic properties of the metastable phase. This approach is based on the extrapolation of the single-phase equation of state into the two-phase domain. The approach was previously proposed for transient water depressurizations (De Lorenzo et al., 2021, 2017), but it has not yet been applied to the DEM. In the end, in order to account for the difference in thermophysical properties between water and organic fluids, a new set of parameters for the DEM constitutive equation is proposed, based on the tuning against experimental data for R134a.

In brief, the novel contributions of this work to the state-of-the-art are:

- The assessment of the applicability of the available one-dimensional models for flashing flows of organic fluids;
- The identification of the most appropriate friction loss correlation for flashing of organic fluids;
- The extension of the applicability of the delayed equilibrium model to high-pressure flows by removing the incompressible flow assumption for the metastable liquid phase;
- The extension of the applicability of the delayed equilibrium model to flashing of organic fluids by tuning the model's constitutive law against experimental data.

The results of this study can be used to improve the modelling of non-equilibrium flashing flows of organic fluids in devices as ejectors, nozzles and expanders, and they can support the optimal design of motive nozzles of the ejectors for heat pumps and refrigeration units and of two-phase expanders for organic Rankine cycle systems and liquefaction units, thereby increasing the performance of these systems.

The paper is structured as follows: Section 2 discusses the phenomena characterizing flashing flows of organic fluids and their similarities and differences with water and CO_2; Section 3 illustrates the methods and the computational framework adopted for the study; in Section 4 a comparison with experimental and numerical results from other authors is provided for validation and verification purposes; in Section 5 the results from available and extended models for R134a are presented and discussed; in Section 6 the conclusions of this work are drawn and recommendations for future investigations are provided.

2. Characteristics of flashing flows of organic fluids

Flashing flows and, more generally, two-phase expansions differ from single-phase flows and present some peculiar features, mainly caused by the presence of macroscopic interfaces dividing phases with different thermo-physical properties. The most important features affecting two-phase flows are the increased frictional pressure gradients due to higher viscous losses compared to those of single-phase flows, the occurrence of non-homogeneous flow conditions, and the presence of non-equilibrium phenomena. Mechanical equilibrium, i.e. pressure equilibrium across the interface between the phases, can be often assumed to be established almost instantaneously, and surface tension effects can be neglected (Bouré et al., 1976). Therefore, throughout this work, the liquid and vapour phase are assumed to share the same pressure field. As it will be discussed in Section 3.1, the higher friction that features flashing flows has been traditionally accounted for through a multiplying factor, namely the Lockhart–Martinelli parameter. The present section provides an overview of the relevant non-equilibrium phenomena in flashing flows of organic fluids and how the thermo-physical properties of the fluid affect non-equilibrium effects and their prediction through the DEM.

2.1. Non-homogeneous conditions

Non-homogenous flow conditions, consisting of a velocity difference between the phases, are seldom observed in flashing flows due to the high velocities involved (De Lorenzo et al., 2017). A velocity difference, or slip, may arise as a result of the different density between the liquid and vapour phases, which tend to be accelerated differently. This effect is counterbalanced by the drag force, which tends to restore a homogeneous velocity for the two phases (Ishii and Hibiki, 2006). A mathematical limit for the slip ratio, i.e. the ratio between liquid and vapour velocity, was derived through a characteristic analysis of the transport equations for mixture models (Tentner and Weisman, 1978) and it applies to all cases where a macroscopic separation between phases cannot be observed. This is usually the case for flashing flows, where the vapour phase appears dispersed into the liquid one (De Lorenzo et al., 2017; Liao and Lucas, 2021). Under this assumption, the mathematical limit for the slip ratio is very close to unity and the phenomenon can be neglected. The validity of this assumption has been confirmed by results obtained with two-fluid models (White, 2022; Zhu and Elbel, 2020), which account for phase separation and have predicted values of the slip ratio very close to unity. Moreover, organic fluids present lower values of density ratio between the phases and higher values of viscosity ratio with respect to water (Fig. 1), resulting in a reduction of the driving force for non-homogeneous conditions and in an increase in the drag force, which reduces velocity gradients between the phases. Therefore, organic fluids are expected to be affected even less by non-homogeneous flow conditions than water, and the homogeneous flow assumption, frequently adopted for water (De Lorenzo et al., 2017), can be extended to this class of fluids with reasonable confidence.

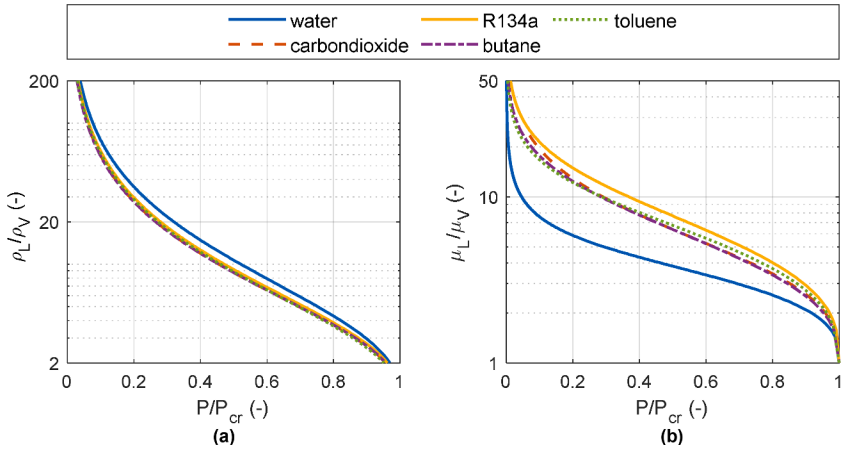

Fig. 1. Evolution of (a) liquid-to-vapour density ratio ρ_L/ρ_V and of (b) liquid-to-vapour dynamic viscosity ratio μ_L/μ_V with reduced pressure P/P_{cr} for different fluids.

2.2. Thermo-chemical non-equilibrium

Thermo-chemical non-equilibrium, characterized by a difference in specific Gibbs energy, or chemical potential (due to the single component considered for these systems), and temperature between the phases, was identified as the main source of non-equilibrium in flashing flows (Liao and Lucas, 2017; Pinhasi et al., 2005). This difference is caused by a delay in the onset of vapour nucleation with respect to saturation conditions, due to the activation energy needed to nucleate the first vapour bubbles, and by the finite heat and mass transfer rate from the liquid to the vapour phase. Due to the delay and reduction of nucleated vapour, which exhibits saturation temperature corresponding to the local pressure, the liquid phase is compelled into metastable conditions, with temperatures exceeding saturation value (superheating). The temperature gradient between the metastable liquid and nucleated vapour persists until a sufficiently high amount of vapour is nucleated and the temperature gradient is completely diffused inside the liquid phase (Bartosiewicz and Seynhaeve, 2013). Therefore, the flow does not reach equilibrium conditions instantaneously after the onset of vapour nucleation. Along the expansion, the two-phase mixture initially constituted by dispersed vapour bubbles eventually evolves in a two-phase flow characterized by dispersed liquid droplets, reaching an asymptotical equilibrium state. In order to evaluate the thermodynamic properties of the two-phase mixture, it is essential to determine the amount of nucleated vapour and of liquid phase evolving in metastable conditions.

The delay in the onset of vapour nucleation determines the temperature gradient, or superheating degree, between the metastable liquid and the saturated phases. The estimation of the nucleation delay is challenging, because of its dependence on the impurities in the flow and at the nozzle walls (Pinhasi et al., 2005). However, the pressure at which nucleation starts, P_{nuc}, has been quantified through the following empirical relation (Lackme, 1979):

$$P_{nuc} = k_{nuc} P_{sat}(T_0) \tag{1}$$

where k_{nuc} is a parameter comprised between 0.95 and 0.98 and T_0 is either the total temperature at the inlet of the nozzle or the temperature at which the flow reaches saturation conditions. The first formulation is usually adopted (De Lorenzo et al., 2017) and was chosen in this study, whereas the latter is more general and can be used also for supercritical conditions at the nozzle inlet.

The delayed equilibrium model relaxes the thermo-chemical equilibrium assumption by considering the two-phase mixture as constituted by 3 phases (Feburie et al., 1993): a saturated vapour phase, a saturated liquid phase and a metastable liquid phase. In fact, upon the nucleation of a vapour bubble, the liquid phase in its proximity is brought to saturation conditions, whereas the bulk of the liquid phase sufficiently far from the nucleated vapour remains in metastable conditions. A schematic representation in the T-s diagram of how the three phases evolve during flashing is provided in Fig. 2. The depicted transformation is isentropic and starts from a generic two-phase condition, but the concept applies also if friction losses are present. Once vapour is nucleated, the vapour phase as well as the saturated liquid phase evolve in equilibrium conditions along the saturated vapour and liquid lines, respectively. The metastable liquid phase, on the contrary, evolves isentropically. The saturated liquid and saturated vapour phases share the same pressure and temperature values, whereas the metastable liquid phase shares only the pressure field with the other phases. If considered incompressible, the metastable liquid phase retains its initial temperature along the expansion. Alternatively, the metastable liquid temperature can be obtained by extrapolating the equation of state within the two-phase domain, as shown in Fig. 2. The final thermodynamic conditions of the mixture can be retrieved by averaging the properties of the three phases, but a unique value of temperature cannot be assigned to the mixture.

The delayed equilibrium model predicts the mass fraction of the mixture in equilibrium conditions γ from the nozzle geometry and the local flow conditions through the following semi-empirical correlation (Feburie et al., 1993):

$$\frac{d\gamma}{dz} = (1-\gamma)\cdot\left(C_1\frac{P_z}{A_z}+C_2\right)\cdot\left[\frac{p_{sat}(T_{L,m})-p}{p_{cr}-p_{sat}(T_{L,m})}\right]^{C_3} \tag{2}$$

where $T_{L,m}$ is the temperature of the metastable liquid phase, $p_{sat}(T_{L,m})$ is the corresponding saturation pressure, p is the pressure of the mixture and p_{cr} is the critical pressure. The parameters C_1 and C_2 are related to the nucleation at the wall and in the bulk flow, respectively. The parameter C_3 is linked to the relationship between temperature and pressure at saturation, which depends on the specific fluid. The values of the parameters C_1, C_2 and C_3 in Eq. (2) were obtained for flashing flows of water and therefore they have to be adjusted to be used for flashing flows of organic fluids.

The volume of the liquid phase evolving in metastable conditions can be directly linked to the volume of nucleated vapour phase and the saturated liquid phase in direct contact with the vapour phase (Pinhasi et al., 2005). The saturated liquid phase is confined to the thermal boundary layer of the vapour phase, which can be correlated with the volume of the vapour phase through the Jakob number, *Ja*. This non-dimensional number accounts for the energy needed to generate the vapour, i.e. the latent heat Δh_{LV}, and for the capacity of the liquid phase to diffuse the temperature gradient between metastable and saturated liquid, $T_{L,m} - T_{sat}(p)$:

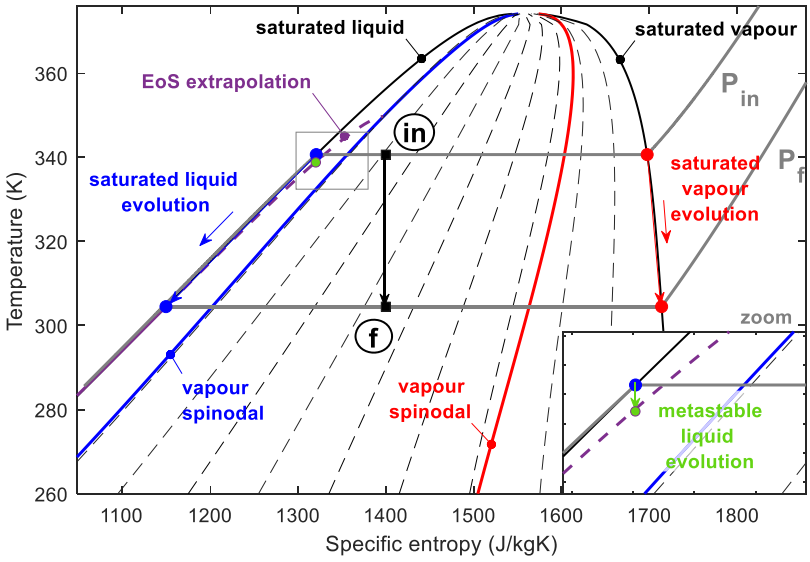

Fig. 2. Schematic representation in the T-s diagram of the evolution of the three phases (saturated liquid in blue, metastable liquid in green, saturated vapour in red) constituting a mixture in initial conditions (in) and final conditions (f) evolving isentropically (fluid: R134a). (For interpretation of the references to colour in this figure legend, the reader is referred to the web version of this article).

$$\mathrm{Ja} = \frac{\rho_L c_{P,L}\left[T_{L,m} - T_{sat}(p)\right]}{\rho_V \Delta h_{LV}} \tag{3}$$

where ρ_L and $c_{P,L}$ are the density and the specific heat capacity of the liquid, respectively, and ρ_V is the density of the vapour.

In thermally controlled bubble evolution, the ratio between thermal boundary layer thickness and bubble radius is inversely proportional to the Jakob number (Pinhasi et al., 2005): $\delta_T/R_B = Ja^{-1}$. As a consequence, the volume fraction of the metastable liquid phase $\varepsilon_{L,m}$ can be expressed as a function of the volume fraction of vapour y and of the Jakob number:

$$\varepsilon_{L,m} = \frac{V_{L,m}}{V} = 1 - y\left(1 + \frac{1}{Ja}\right)^3 \tag{4}$$

Fig. 3a shows the distribution of the Jakob number (divided by the temperature difference between metastable and saturated liquid, $\Delta T = T_{L,m} - T_{sat}(p)$, in order to make it dependent only on the thermophysical properties of the fluid) with the reduced pressure, P/P_{cr}. Organic fluids as R134a, butane, and toluene show similar values of the Jakob number, but differ from water and CO_2. Overall, the Jakob number is lower for water and therefore, according to Eq. (4), the volume fraction of metastable liquid is lower for water than for organic fluids under the same temperature difference between metastable and saturated liquid. For pressures close to the critical point, approximately $P > 0.9 \cdot P_{cr}$, the Jakob number decreases despite the sharp increase of $Ja/\Delta T$, because the temperature difference between saturated and metastable liquid tends to 0. This tendency can be observed when computing the metastable liquid temperature extrapolating the equation of state into the two-phase region, whereas adopting the incompressible assumption for the metastable liquid prevents capturing this behaviour. For this reason, the DEM in its original formulation is not suited for pressures close to the critical point, as found for CO_2 (Angielczyk et al., 2020).

The relation between pressure and temperature at saturation, or saturation law, appears in the last term of the constitutive law of the DEM: $\left[\frac{p_{sat}(T_{L,m}) - p}{p_{cr} - p_{sat}(T_{L,m})}\right]^{C_3}$. In this regard, organic fluids differ from one another, as shown by Fig. 3b. The R134a's saturation law appears to be very close to water's, while butane's saturation law is close to CO_2's. However, the saturation law index can be directly used to adapt the DEM correlation to the adopted fluid, whereas the dependence on the Jakob number is difficult to retrieve from the correlation. For this reason, and

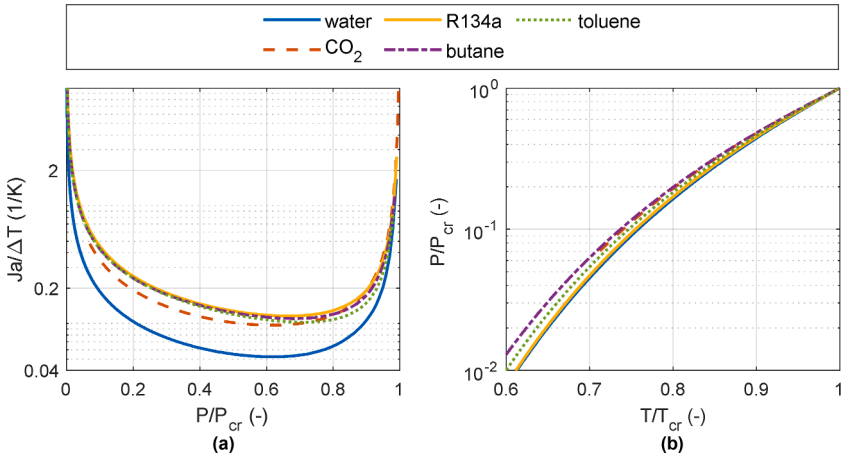

Fig. 3. Evolution of (a) Jakob number divided by the temperature difference between metastable and saturated liquid with reduced pressure and of (b) reduced pressure at saturation with reduced temperature for different fluids.

because the R134a and water have a similar saturation law, the tuning of the DEM correlation performed in this study focuses on the parameters C_1 and C_2, and not on the term related to the saturation law.

3. Methods

3.1. One dimensional model

The one-dimensional model adopted in this work is a homogeneous mixture model based on the delayed equilibrium formulation and it is a further development of the one-dimensional homogenous equilibrium model presented by the same authors (Tammone et al., 2023). The model is implemented in MATLAB (2022) and solves, under steady-state conditions, for the equations of continuity (Eq. (5)), momentum (Eq. (6)), and energy (Eq. (7)) in their conservative form by using a finite volume discretization.

$$\frac{\Delta(\rho \mathrm{vA})}{\Delta \mathrm{z}} = 0 \tag{5}$$

$$\frac{\Delta(\rho \mathrm{vA}\cdot \mathrm{v})}{\Delta \mathrm{z}} + \frac{\Delta(\mathrm{pA})}{\Delta \mathrm{z}} - \frac{\mathrm{pA_w}\sin(\vartheta)}{\Delta \mathrm{z}} + \frac{\tau_\mathrm{w}\mathrm{A_w}\cos(\vartheta)}{\Delta \mathrm{z}} = 0 \tag{6}$$

$$\frac{\Delta[\rho \mathrm{vA}\cdot(\mathrm{h} + \mathrm{v}^2/2)]}{\Delta \mathrm{z}} = 0 \tag{7}$$

where τ_w is the equivalent two-phase wall shear stress, ϑ is the opening angle of the converging or diverging section of the nozzle, A is the cross section area and A_w is the area of the lateral wall surface. The equivalent wall shear stress is evaluated using empirical correlations through the Lockhart–Martinelli approach. This approach is based on the observation that in two-phase flows shear stresses are higher than in single-phase flows due to friction forces exerted by each phase on the other one. This effect is modelled using the Reynolds number of the liquid phase, comprising the saturated and metastable liquid fractions, to evaluate the friction factor and a multiplying factor, or Lockhart–Martinelli parameter, Φ_{LM}, to obtain the two-phase shear stress, τ_w, from the value calculated for the single phase, $\tau_{w,L}$:

$$\tau_\mathrm{w} = \Phi^2_\mathrm{LM}\cdot\tau_\mathrm{w,L} \tag{8}$$

$$\tau_\mathrm{w,L} = \frac{1}{2}\mathrm{C_{f,L}}\frac{\mathrm{G_L^2}}{\rho_\mathrm{L}} \tag{9}$$

where $C_{f,L}$ is the liquid friction factor calculated from the Colebrook-White correlation (Clamond, 2009) using the liquid Reynolds number computed assuming that the liquid flows alone in the duct: $Re_L = G_L D_L / \mu_L$, with $G_L = \dot{m}_L/A$. Several correlations for the Lockhart–Martinelli parameter have been proposed. For water, Richardson's correlation (Richardson, 1958) has been mainly adopted (De Lorenzo et al., 2017), whereas for CO_2 flows Friedel's correlation (Friedel, 1979) was deemed more suitable (Angielczyk et al., 2019). In this paper, the correlation from Grönnerud (1972), which was developed for refrigerants and is considered the most suitable for organic fluids (Ould Didi et al., 2002), and the correlations from Beattie (1973) and Chisholm (1973) are also evaluated to identify the most suitable correlation for organic fluids. A detailed summary of the empirical correlations used for the Lockhart–Martinelli parameter is provided in Appendix A.1.

The fluid domain is discretized through control volumes that are delimited by the lateral surface (A_w) representing the walls of the nozzle and by the cross sections (A), at the generic locations z and $z + \Delta z$, where all the properties are evaluated. In this study, the nozzle is discretized in $N = 50$ control volumes for the converging, straight and diverging sections, with a refinement near the critical section, i.e. the throat section, where the highest gradients are expected. The refinement follows a geometrical progression, as in De Lorenzo et al. (2017):

$$\Delta \mathrm{z_i} = \frac{\mathrm{L}(1-\mathrm{d})}{1-\mathrm{d}^{\mathrm{N}+1}}\mathrm{d}^{\mathrm{i}-1} \tag{10}$$

where L is equal to the length of the considered section and d is a parameter that controls the grid refinement and it is chosen to have uniform pressure gradients across the control volumes along the nozzle. For the diverging section a value of $d = 1.1$ is used, whereas for the converging and straight section a value equal to $d = 0.85$ is used in all cases except for the Moby Dick nozzle for which the value $d = 0.97$ is adopted. The grid refinement is adjusted through a sensitivity analysis, whose results are reported in detail in Appendix A.2.

3.2. Two-phase mixture properties

The model adopted in this paper treats the fluid as a mixture, whose thermodynamic and transport properties are defined by averaging the properties of the liquid (saturated and metastable) and vapour phases. The DEM introduces an additional variable, the mass fraction of mixture in equilibrium conditions γ, which is evaluated through an empirical correlation, Eq. (2). The mass and volume fraction of the three phases considered in the DEM are defined over the total mass and total volume of the mixture, respectively. In addition, the volume fraction of the vapour phase, or void fraction, y is used to characterize the composition of the mixture. A summary of the mass and volume fractions is reported in Table 1, together with the relations among the quantities.

Mass-specific properties as specific enthalpy h, specific entropy s and specific volume ν of the mixture are computed based on a mass-weighted average, whereas volume-specific properties as the density ρ and properties related to transport phenomena across volumes, as conductivity k and dynamic viscosity μ, are computed based on a volume-weighted average, following Romei and Persico (2021) and De Lorenzo et al. (2017):

$$\begin{cases} \psi = x\cdot\psi_{\mathrm{V,sat}} + (\gamma - \mathrm{x})\cdot\psi_{\mathrm{L,sat}} + (1-\gamma)\cdot\psi_{\mathrm{L,m}} \ \textit{if}\ \psi = h, s, \nu \\ \psi = y\cdot\psi_{\mathrm{V,sat}} + \varepsilon_{\mathrm{L,sat}}\cdot\psi_{\mathrm{L,sat}} + \varepsilon_{\mathrm{L,m}}\cdot\psi_{\mathrm{L,m}} \ \textit{if}\ \psi = \rho, k, \mu \end{cases} \tag{11}$$

The saturation properties and the metastable properties are retrieved from look-up tables to reduce the computational cost. The look-up tables for saturation properties are one-variable functions and are compiled with the saturation pressure as independent variable. The look-up tables for metastable properties are two-variable functions and use the pressure and the specific entropy as independent variables. The pressure is varied between the triple point and the critical point for both saturation and metastable properties look-up tables, and a uniform discretization in 10^5 and 10^3 points is adopted respectively. For the metastable properties, the entropy was varied between the saturated liquid and saturated vapour value at the triple point with a uniform discretization in 10^3 points. The resulting relative error in the derived thermodynamic properties with respect to the value provided directly by the equation of state is lower than 10^{-6} and 10^{-4} for saturation and metastable look-up tables, respectively. All thermodynamic properties outside the two-phase domain are retrieved directly from the CoolProp library (Bell et al., 2014), which adopts the equation of state in terms of the fundamental Helmholtz free energy relation (HEOS). Previous works treated the metastable liquid phase as incompressible and isentropic (Angielczyk et al., 2020; De Lorenzo et al., 2017). In this work, the metastable

Table 1
Mass and volume fraction of the three phases of the DEM referred to the mass and volume flow rate of the mixture, respectively.

	Mass fraction	Volume fraction
Saturated liquid	$\gamma - x$	$\varepsilon_{L,sat} = (\gamma - x)\frac{y}{x}\frac{\rho_{V,sat}}{\rho_{L,sat}}$
Metastable liquid	$1 - \gamma$	$\varepsilon_{L,m} = (1-\gamma)\frac{y}{x}\frac{\rho_{V,sat}}{\rho_{L,m}}$
Saturated vapour	x	y

phase is not considered incompressible and the thermodynamic properties are computed by extrapolating the single-phase equation of state within the two-phase domain without imposing chemical equilibrium. The density and enthalpy of the metastable phase are then computed assuming isentropic evolution of the metastable phase. Making an assumption on the transformation of the metastable phase is necessary, as two thermodynamic quantities are needed for the evaluation of its state.

The system of Eqs. (5)–(7) is numerically solved for the mixture velocity (v), the pressure shared by the three phases (P), and the mixture specific entropy (s). The pressure is used to retrieve the saturation properties of the three phases, whereas the specific entropy of the mixture s is used to calculate the composition of the mixture in terms of vapour quality x through the mass-specific property definition:

$$s = x \cdot s_{V,sat} + (\gamma - x) \cdot s_{L,sat} + (1 - \gamma) \cdot s_{L,m} \tag{12}$$

where the specific entropy of the metastable liquid phase $s_{L,m}$ is constant and equal to the entropy of the liquid phase at the onset of nucleation and the mass fraction of the mixture in equilibrium conditions γ is given by integrating numerically the constitutive law of the DEM expressed by Eq. (2). In this work, the set of coefficients C_1, C_2 and C_3 proposed by Bartosiewicz and Seynhaeve (2013) for water is initially adopted and read as:

$$\begin{cases} C_1 = 0.00839 \\ C_2 = 0.63369 \\ C_3 = 0.22813 \end{cases} \tag{13}$$

The parameters C_1 and C_2 have been then tuned to find the most suitable set for the considered fluid and flow conditions (see Section 5.4 for the details), whereas the parameter C_3 is set to the values suggested for water, for the similarity between R134a and water in terms of relationship between pressure and temperature at saturation, discussed in Section 2.

In this work, the speed of sound does not have a role in the determination of the critical conditions due to the solution procedure adopted (Section 3.3), and therefore its definition does not affect the results of the simulations.

3.3. Solution procedure

To solve the flow in the converging-diverging nozzle, boundary conditions have to be assigned at the inlet and at the outlet. The outlet boundary conditions are assigned is terms of static pressure and they are used when the flow is not choked to obtain the subsonic solution. At the inlet, boundary conditions are assigned as stagnation properties and the mass flow rate (or, alternatively, the mixture velocity) has to be assumed to find the static conditions. In this work, the flow is solved iteratively to find the critical mass flow rate, i.e. the maximum mass flow rate that the nozzle can convey, or the mass flow rate matching the imposed boundary conditions at the outlet. The computational time for the solution of the flow along the nozzle is approximately 1 minute, whereas the calculation of the critical mass flow rate requires approximately 20 min.

A dedicated algorithm to find the critical mass flow rate is used in this work, based on the approach suggested by Bouré et al. (1976) and adopted by several authors (Angielczyk et al., 2020, 2019; De Lorenzo et al., 2017). Fig. 4 provides a schematic representation of the algorithm. The critical mass flow rate and the corresponding choked subsonic and adapted supersonic solutions are always computed first. Thereafter, the subsonic unchoked solution can be calculated if the imposed outlet pressure is higher than the outlet pressure for the subsonic choked solution. In fact, a lower outlet pressure cannot be imposed without admitting the presence of shock waves or expansion waves within or outside the nozzle. The residual e used during the iterations differs for the two solutions, i.e. "critical flow" and "subsonic flow", and it corresponds to the choking condition for the first and to the error on the outlet pressure for the latter.

To evaluate the residuals, the solution along the nozzle axis is computed on each section following a forward-marching scheme. As previously mentioned and shown on the right-hand side of Fig. 4, the system of Eqs. (5)–(7) is solved using static pressure (p), mixture specific entropy (s) and velocity (v) as independent variables. The continuity and momentum equations are solved implicitly to find the pressure and the mixture specific entropy respectively, whereas the energy equation is explicitly solved to retrieve the mixture velocity. On every section of the nozzle the system of equations has always two solutions, namely a subsonic one and a supersonic one. The first is found for lower values of

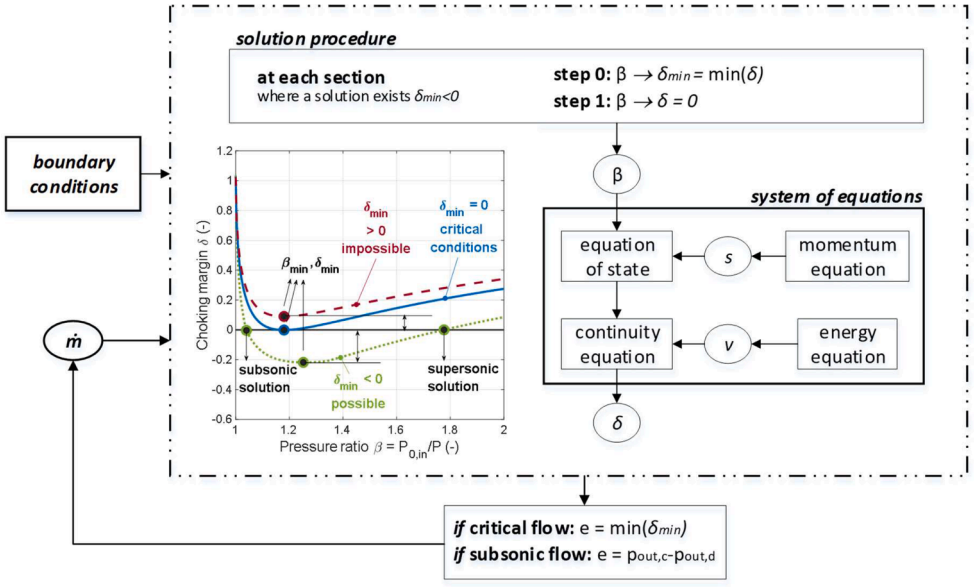

Fig. 4. Flow diagram representing the solution procedure when solving for critical or subsonic flow conditions, including a plot showing the evolution of the choking margin with the pressure ratio for the possible types of solutions that can be encountered on each section of the nozzle: impossible flow solution in red, critical flow solution in blue and subcritical flow solution in green. (For interpretation of the references to colour in this figure legend, the reader is referred to the web version of this article).

the pressure ratio $\beta = P_{0,in}/P$ and the latter for higher values. To limit the range of variation of the pressure, the choking conditions on the section are computed ("step 0") by minimizing the residual of the continuity equation δ:

$$\delta = 1 - \frac{\rho v A}{\dot{m}} \tag{14}$$

Then, the range of variation of pressure is assigned depending on the searched solution, i.e. subsonic or supersonic, and the flow is solved by searching the zero of the continuity equation residual δ ("step 1"). The residual δ is also called choking margin, as it represents the distance of the flow from choking conditions, as shown in the plot on the left-hand side of Fig. 4. The latter depicts the distribution of the choking margin with pressure ratio for different types of solutions on a section along the nozzle axis. If the assigned mass flow rate value is below or equal to the critical one (green dotted line in Fig. 4), a subsonic and a supersonic solution can be found at every section up to the outlet of the nozzle. On the contrary, if the assigned mass flow rate value is above the critical one, the solver will find a section where no solution is found (red dashed curve in Fig. 4) and it will stop solving before reaching the outlet section of the nozzle. In this case, the algorithm corrects the value of the assigned mass flow rate to bring the residual e under the imposed tolerance. Once the choking mass flow rate and the choking section, i.e. the section where the choking margin is zero, are identified, the supersonic solution can be computed by imposing the mass flow rate equal to the critical value and by limiting the range of variation of pressure to the supersonic one for the sections downstream the choking section. Retrieving the position of the choking section is necessary because, differently from isentropic flows, the choking section is found downstream of the throat section when viscous losses are present. As a matter of fact, the negative pressure gradient due to friction losses has to be balanced by a positive pressure gradient due to area change in order to have choking conditions and this happens in locations downstream of the throat. As the friction losses increase and as the opening angle of the diverging section decreases, the choking section is found further downstream of the throat. Eventually, the flow may choke at the nozzle outlet for very high frictional losses, as observed for flashing CO_2 in nozzles of small size (Nakagawa et al., 2009).

3.4. Experimental data and cases studies

In this study, experimental and numerical data for water (De Lorenzo et al., 2017) ("MD cases"), CO_2 (Angielczyk et al., 2019; Nakagawa et al., 2009; Romei and Persico, 2021) ("NA cases") and R134a (Zhu and Elbel, 2019) ("ZE cases") are considered as benchmarks for comparison with the numerical results. The geometry of the nozzles investigated in this work is summarized in Table 2. MD and ZE nozzles are axisymmetric. NA nozzle has a rectangular cross section with a width-to-throat ratio of 12.5, thus expecting a two-dimensional flow configuration therein. NA and ZE nozzles have a conical shape, whereas the MD nozzle has a smooth converging section, as shown in Fig. 5a. An overview of the boundary conditions for the various case studies considered is provided in Tables 3–5. The MD and NA cases are choked flows, as reported by the authors. For this reason, the pressure at the nozzle outlet is not used as boundary condition in this study and the critical solution is calculated instead. On the contrary, ZE cases are subsonic flows and the outlet pressure was imposed.

The case studies considered in this work are represented in the T-s diagram in Fig. 6 with their total inlet and isentropic outlet boundary conditions. For the NA nozzles, the pressure at the last pressure tap was used, as the pressure was not measured at the nozzle outlet. When a pressure value below the triple point was measured, the outlet pressure was set to the triple point pressure. For the ZE cases, the expansion occurs mainly between the saturation line and the spinodal line and therefore non-equilibrium effects are expected to be particularly significant.

While comparing experimental data and numerical results, the following definition of the root mean square relative error $e_{\phi,RMSR}$ and the relative error $e_{\phi,R}$ are adopted:

$$e_{\phi,RMSR} = \sqrt{\frac{1}{n}\sum_{i=1}^{n}\left(\frac{\phi_i - \phi_{exp,i}}{\phi_{exp,i}}\right)^2} \tag{15}$$

$$e_{\phi,R} = \frac{\phi_i - \phi_{exp,i}}{\phi_{exp,i}} \tag{16}$$

where ϕ_i and $\phi_{exp,i}$ are the numerical and experimental value of the considered variable and n is the number of considered points. The propagated experimental uncertainty on the root mean square error is evaluated as:

$$\Delta e_{\phi,RMSR} = \sqrt{\sum_{i=1}^{n}\left[\left(-\frac{1}{n}\frac{\phi_i(\phi_i - \phi_{\exp,i})}{{\phi_{\exp,i}}^3 e_{\phi,RMSR}}\right)^2 {\Delta\phi_{\exp,i}}^2\right]} \tag{17}$$

where $\Delta\phi_{exp,i}$ is the experimental uncertainty.

4. Validation and verification

The results from the proposed 1D model with the HEM approach and the original DEM approach (DEM0) are here compared with results from 1D models from other authors and experimental data in order to verify the consistency of the adopted model. The fluids previously investigated and considered in this section are water and CO_2.

4.1. Carbon dioxide

A comparison of the proposed model adopting the HEM and the state-of-the-art DEM with results from a 1D HEM and a 1D DEM documented in literature (Angielczyk et al., 2019) is shown in Fig. 7. The comparison shows an excellent agreement of the 1D HEM used in this study with the one documented in the literature. For the DEM, the

Table 2
Geometrical details of the nozzles used in this work: MD nozzles from De Lorenzo et al. (2017), NA nozzles from Nakagawa et al. (2009) and ZE nozzles from Zhu and Elbel (2019).

	Radius			Length			
	inlet R_1 (mm)	throat R_2 (mm)	outlet R_3 (mm)	converging L_1 (mm)	straight L_2 (mm)	diverging L_3 (mm)	roughness k_s (μm)
MD	33.53	10	15.44	100	363.55	-	9.4
NA b	5.00	0.12	0.27	27.35	0	56.15	6.2
NA c	5.00	0.12	0.42	27.35	0	56.15	6.2
NA d	5.00	0.12	0.72	27.35	0	56.15	6.2
ZE a	7.50	0.51	0.685	9.9	0	20.0	9.4
ZE b	7.50	0.415	0.595	9.9	0	20.0	9.4
ZE c	7.50	0.5	0.59	9.9	0	20.0	9.4

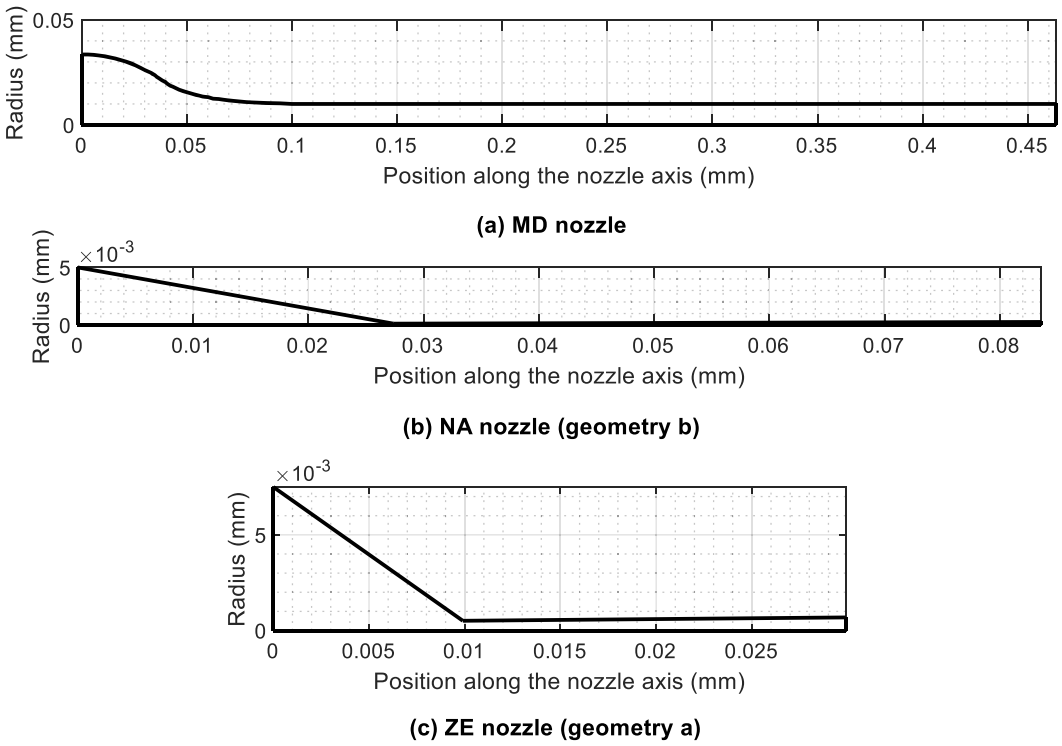

Fig. 5. Geometry of the nozzles considered in this study.

Table 3
Boundary conditions for the cases investigated with Moby Dick experiment (De Lorenzo et al., 2017) with water. Thed at the inlet.

Name	geom	$P_{0,in}$ (bar)	$T_{0,in}$ (K)
MD-20a	a	20	421.65
MD-20b	a	20	440.25
MD-20c	a	20	466.25
MD-20d	a	20	485.45
MD-120a	a	120	578.95
MD-120b	a	120	592.55

Table 4
Boundary conditions for the cases experimentally investigated by Nakagawa et al. (2009) with CO2. At the inlet, the flow is supercritical for NA-9b and NA-9d, while it is subcooled liquid for the other cases.

Name	geom	$P_{0,in}$ (bar)	$T_{0,in}$ (K)
NA-9b	b	91	310.45
NA-9d	d	91	309.65
NA-7d	d	71	299.55
NA-6b	b	61	293.15
NA-6c	c	61	294.95

agreement between the results from the model adopted in this study and the results from Angielczyk et al. (2019) is worse, because of the lack of information on the adopted friction model and delay in the onset of nucleation.

For case NA-6c, where the pressure distribution along the axis is dominated by friction effects, the results from the HEM suggest that the adopted friction models are not suitable. On the contrary, the results from the HEM follow closely the experimental pressure distribution in case NA-7d and NA-9d, where the pressure distribution is primarily influenced by the area gradients. In both cases, the results indicate that the proposed model with HEM assumption and Friedel's correlation

Table 5
Boundary conditions for the cases experimentally investigated by Zhu and Elbel (2019) with R134a. At the inlet, the flow is subcooled liquid for cases ZE-1 to ZE-7 and in two-phase conditions for case ZE-10.

Name	geom	$P_{0,in}$ (bar)	$T_{0,in}$ (K)	$x_{0,in}$ (-)	P_{out} (bar)
ZE-1	a	9.25	309.15	-	6.15
ZE-2	a	9.25	309.15	-	6.80
ZE-3	a	10.35	313.15	-	6.80
ZE-4	b	9.25	309.15	-	6.15
ZE-5	b	10.35	313.15	-	6.80
ZE-6	c	9.25	309.15	-	6.80
ZE-7	c	9.25	309.15	-	6.80
ZE-10	a	9.25	309.15	0.022	6.80

underpredicts the friction losses, whereas Richardson's correlation better predicts the pressure distribution and the mass flow rate, as shown in Table 6. The importance of the frictional pressure gradients caused by the high values of relative wall roughness is also confirmed by the 2D CFD results, displayed in Fig. 8, which suggest that the wall roughness has to be taken into account to match accurately the experimental pressure profile.

The small discrepancy between the HEM and the experimental data observed for case NA-6b can be attributed to the presence of slight thermal non-equilibrium effects, which are not present in case NA-9b due to the proximity to the critical point. However, the adoption of the DEM could not improve significantly the prediction of the pressure profile, since the adopted DEM correlation was formulated for flashing of water at lower reduced pressures and does not predict sufficiently high non-equilibrium effects at the pressure levels of case NA-6b.

4.2. Water

Although several sets of experimental data are available for flashing water, a comparison with experimental data from the Moby Dick experiment is here presented, as it has been already used as benchmark

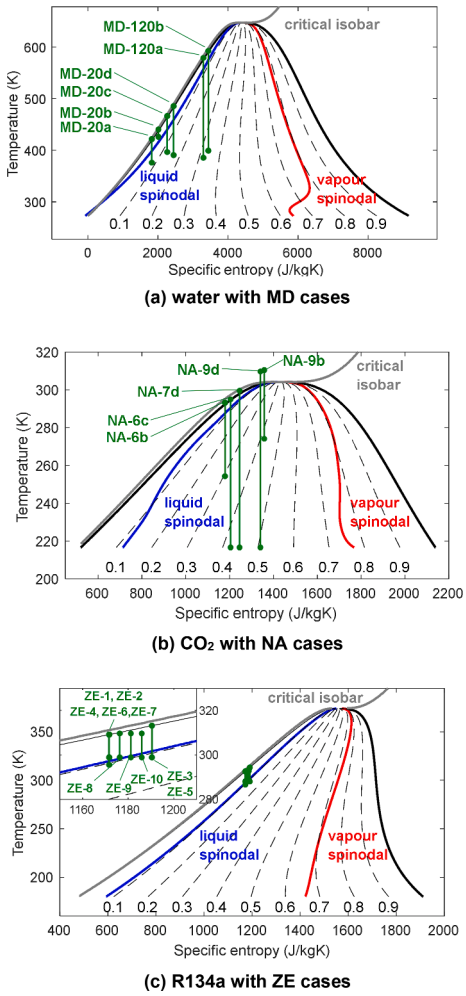

Fig. 6. T-s diagrams of the fluids and cases studies, indicated as isentropic processes, considered in this work.

with the 1D DEM developed for water (De Lorenzo et al., 2017). Figs. 9 and 10 show a comparison of the proposed model with experimental and numerical results from a previous study (De Lorenzo et al., 2017) in terms of pressure and void fraction distribution. The results suggest that the proposed model adopting the original DEM (DEM0) is consistent with numerical results from the literature and it is able to predict the experimental data very closely. The small difference between the results was attributed to the lack of information on the roughness levels and computational grid adopted by De Lorenzo et al. (2017).

5. Results for R134a and discussion

5.1. Influence of friction loss formulation

The prediction of the frictional pressure gradient is crucial for flashing flows, especially when Reynolds numbers are small, as in lab-scale facilities. In fact, as highlighted in Section 3.3, the frictional pressure gradient determines the position of the choking section, which can be found at the exit of the nozzle for high frictional pressure gradients. In addition, previous works (Angielczyk et al., 2019; De Lorenzo et al., 2017; Ould Didi et al., 2002) have shown that the optimal friction loss correlation can change depending on the fluid and operating conditions. In this work, a number of different available correlations were tested with the HEM in order to select the most appropriate ones for flashing flows of R134a. The results in Fig. 11 suggest that the correlations for the Lockhart–Martinelli parameter proposed by Grönnerud (1972), Friedel (1979), Beattie (1973) and Chisholm (1973) give very similar results. For cases ZE-2 and ZE-10, the flow is dominated by friction losses, with a continuous expansion in the diverging section of the nozzle despite the subsonic conditions. For these cases, only Richardson's correlation (Richardson, 1958) is able to predict the expected pressure trend in the diverging section.

However, Richardson's correlation fails to predict the pressure trend for flows dominated by area gradient effects, as in case ZE-7. In this case, the Richardson correlation overpredicts the losses after the throat, where the flow undergoes first a further expansion in supersonic conditions before resuming subsonic conditions due to the increased frictional pressure gradients in the final portion of the diverging nozzle. In

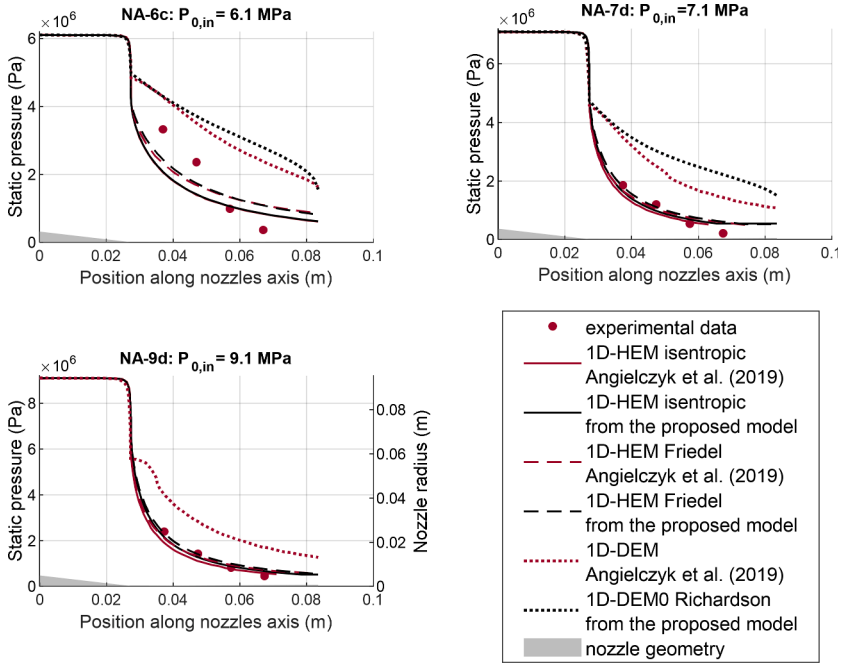

Fig. 7. Comparison between experimental data (Nakagawa et al., 2009) and pressure profiles obtained by Angielczyk et al. (2019) and with the proposed 1D-HEM and 1D-DEM with isentropic assumption and Friedel's and Richardson's correlation for the Lockhart–Martinelli parameter.

Table 6
Comparison between mass flow rates computed by Romei and Persico (2021) with 2D-CFD adopting the HEM and different approaches for the wall roughness and the proposed 1D-HEM and 1D-DEM with Richardson and Friedel correlations for the Lockhart–Martinelli parameter.

(kg/s)	2D-CFD-HEM rough walls wall functions	2D-CFD-HEM smooth walls wall functions	1D-HEM isentropic	1D-HEM Richardson	1D-HEM Friedel	1D-DEM0 Richardson
NA-6b	0.02226	0.02496	0.02530	0.02134	0.02438	0.02409
NA-9b	0.02832	0.03234	0.03256	0.02788	0.03215	-

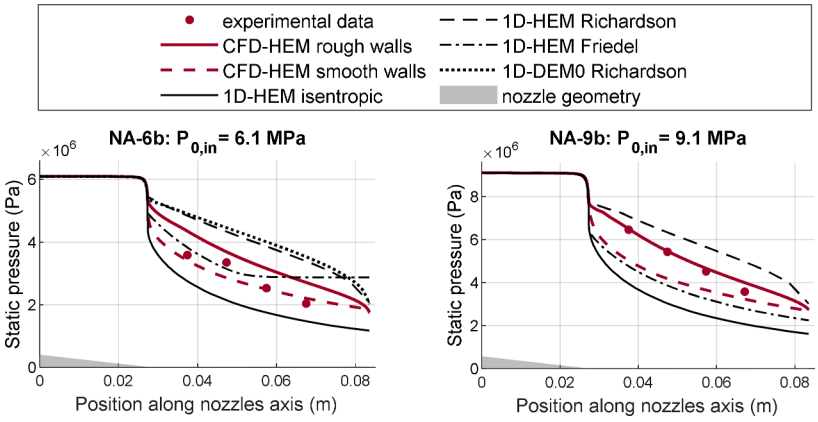

Fig. 8. Comparison between experimental data (Nakagawa et al., 2009) and pressure profiles obtained by Romei and Persico (2021) with 2D-CFD adopting the HEM and the proposed 1D-HEM and 1D-DEM with Richardson and Friedel correlations for the Lockhart–Martinelli parameter.

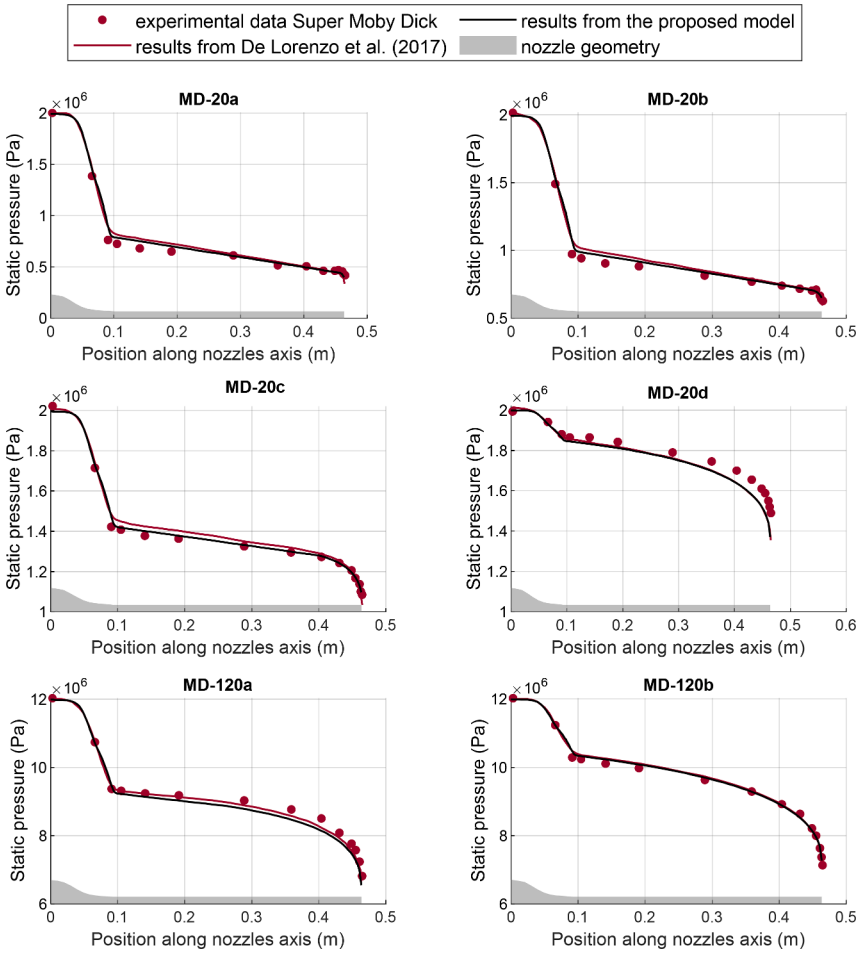

Fig. 9. Comparison in terms of pressure profiles between experimental data from the Moby Dick experiment (De Lorenzo et al., 2017) and numerical results obtained with a 1D-DEM by De Lorenzo et al. (2017) and with the proposed 1D-DEM0 using Richardson correlation for the Lockhart–Martinelli parameter.

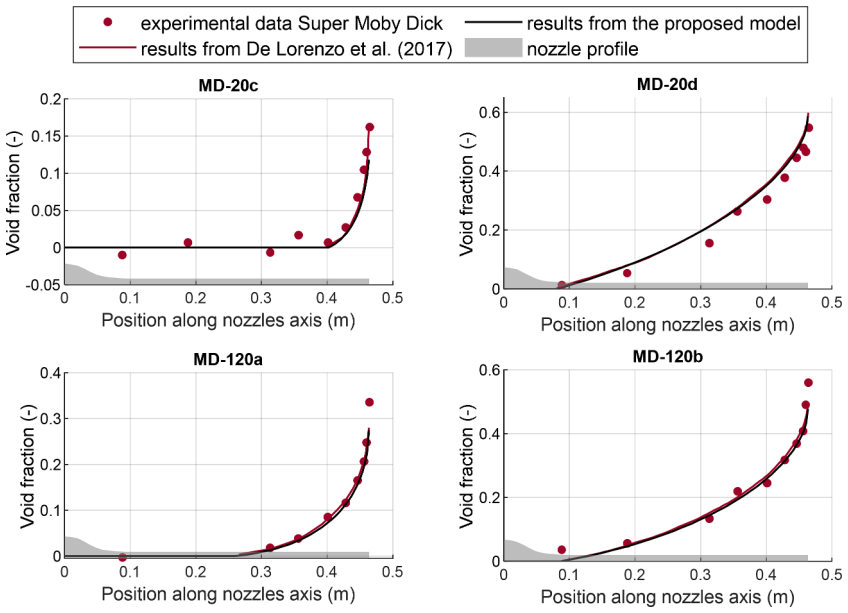

Fig. 10. Comparison in terms of void fraction profiles between experimental data from the Moby Dick experiment (De Lorenzo et al., 2017) and numerical results obtained with a 1D-DEM by De Lorenzo et al. (2017) and with the proposed 1D-DEM0 using Richardson correlation for the Lockhart–Martinelli parameter.

addition, for case ZE-7 the predicted throat pressure at the choking mass flow rate is significantly higher than the experimental one, which indicates that the HEM is not able to predict the choking conditions appropriately. In fact, the sensitivity of the throat pressure to the vaporization rate increases close to choking conditions, as the influence of non-equilibrium effects on the compressibility of the flow increases. For this reason, both Grönnerud's and Richardson's friction correlations were later adopted together with the DEM, also considering that Grönnerud's correlation was specifically developed for refrigerants (Ould Didi et al., 2002).

5.2. Comparison of HEM and original DEM for R134a

The original DEM with a pressure at the onset of nucleation defined by Eq. (1), with $k_{nuc} = 0.95$, was initially adopted to verify whether the model is suitable for flashing flows of R134a. A comparison between the results from the HEM and the original DEM formulation (DEM0), is presented in Fig. 12 for various cases with subcooled liquid inlet conditions. The case with two-phase conditions at the nozzle inlet (ZE-10) is not included hereafter, as the DEM was originally developed for flashing from inlet subcooled conditions (Feburie et al., 1993). As opposed to what was concluded for the HEM in Section 5.1, the results indicate that Grönnerud's correlation for the Lockhart-Martinelli parameter predicts better the pressure profile for all the cases where the frictional pressure gradient is predominant (ZE-1 to ZE-6) when adopting the DEM. For case ZE-7, which is governed by the area gradient, the Grönnerud correlation underpredicts the pressure at the throat and the losses in the diverging section, whereas Richardson's correlation yields a better prediction of the pressure profile. Overall, the original DEM gives a better prediction of the pressure distribution for all cases with respect to the HEM. The

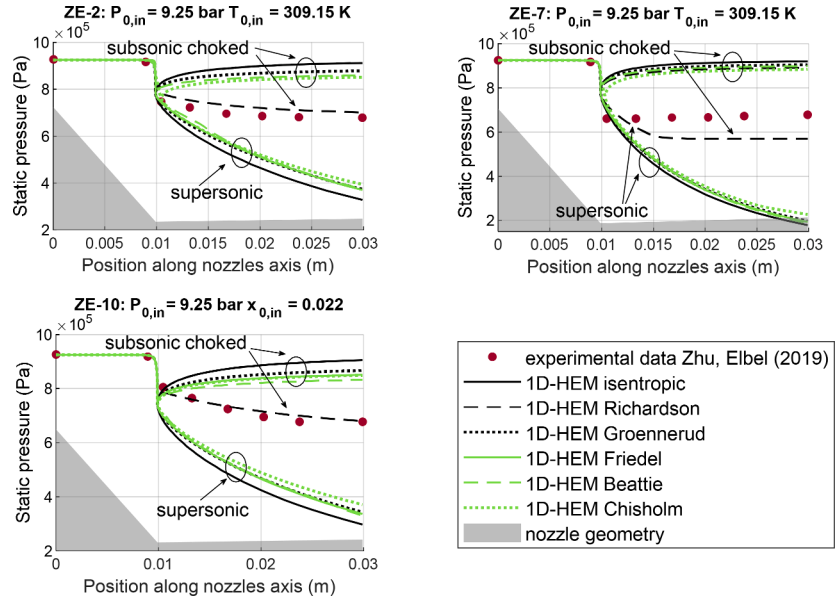

Fig. 11. Comparison between experimental data (Zhu and Elbel, 2019) and results from the 1D-HEM with different correlations for the Lockhart–Martinelli parameter for cases ZE-2, ZE-7 and ZE-10. The reported uncertainty for pressure measurements is ±0.02 bar.

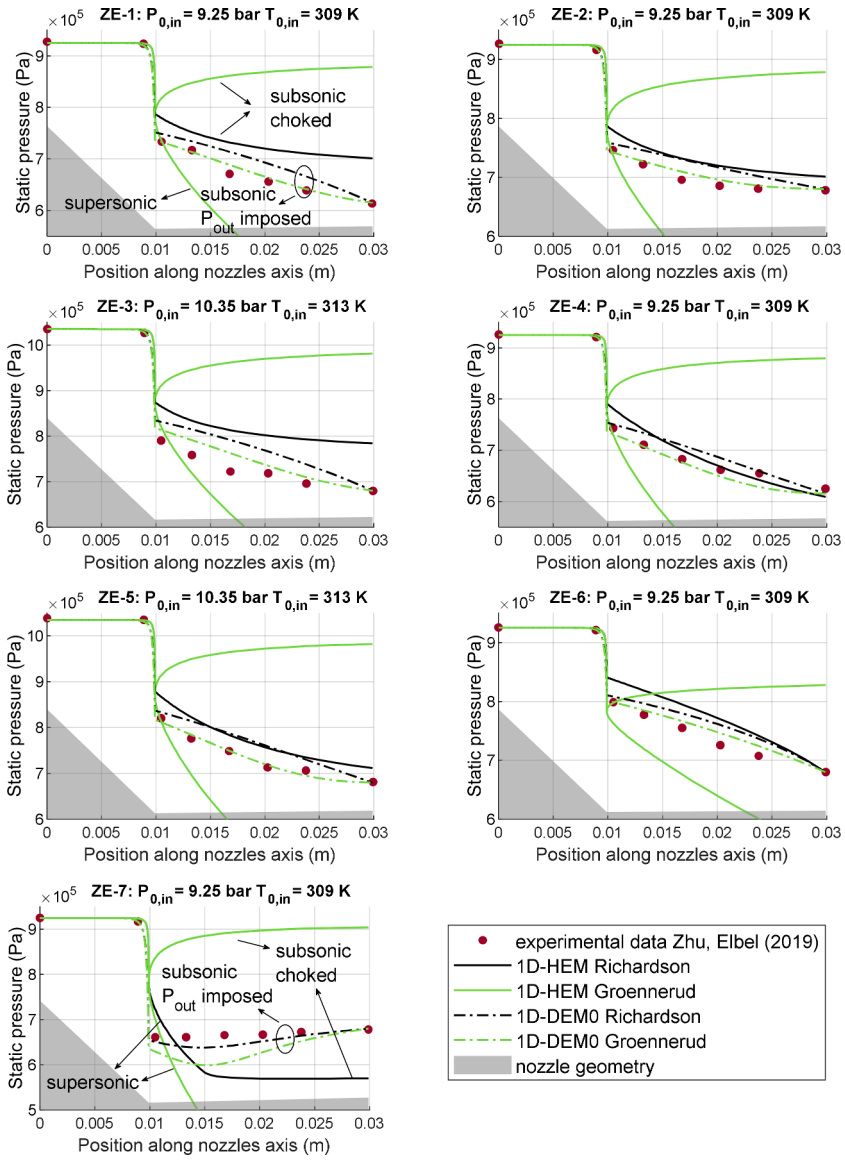

Fig. 12. Comparison between experimental data (Zhu and Elbel, 2019) and results from the 1D-HEM and the original 1D-DEM (DEM0) with for cases from ZE-1 to ZE-7. The reported uncertainty for pressure measurements is ±0.02 bar.

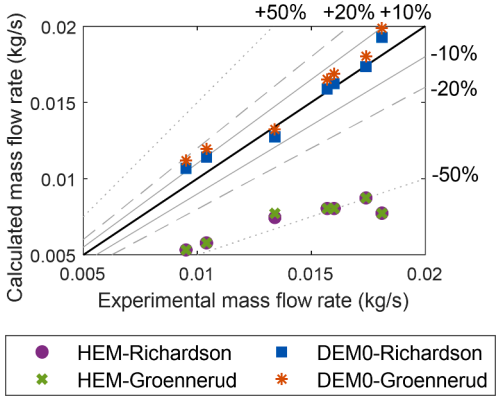

Fig. 13. Comparison between measured (Zhu and Elbel, 2019) and calculated mass flow rate with the 1D-HEM and the original 1-DEM (DEM0) for cases from ZE-1 to ZE-7. The reported uncertainty for mass flow rate measurements is $\pm 10^{-4}$ kg/s.

Table 7
Root mean square relative error for mass flow rate calculated with the 1D-HEM and the original 1D-DEM (DEM0). .

	HEM Richardson	HEM Grönnerud	DEM0 Richardson	DEM0 Grönnerud
$e_{m,RMSR}$ (-)	0.486	0.483	0.069	0.103
$\Delta e_{m,RMSR}$ (-)	0.001	0.001	0.004	0.004

comparison between measured and predicted mass flow rates with the same models is shown in Fig. 13. As already found in Tammone et al. (2023), the results suggest that the HEM strongly underpredicts the mass flow rate by up to 57.3 % in maximum relative error (Eq. (16)), with the largest deviations occurring for the flows closer to choking conditions and dominated by the area gradient (case ZE-7). The DEM0 with Richardson's correlation gives a slightly better prediction of the mass flow rate with respect to Grönnerud's correlation, with a maximum relative error, as defined by Eq. (16), of 12.4 % and 17.8 %, respectively, and a root mean square relative error, as in Eq. (15), of 6.9 % and 10.3 %, respectively (Table 7). The lower values of mass flow rates

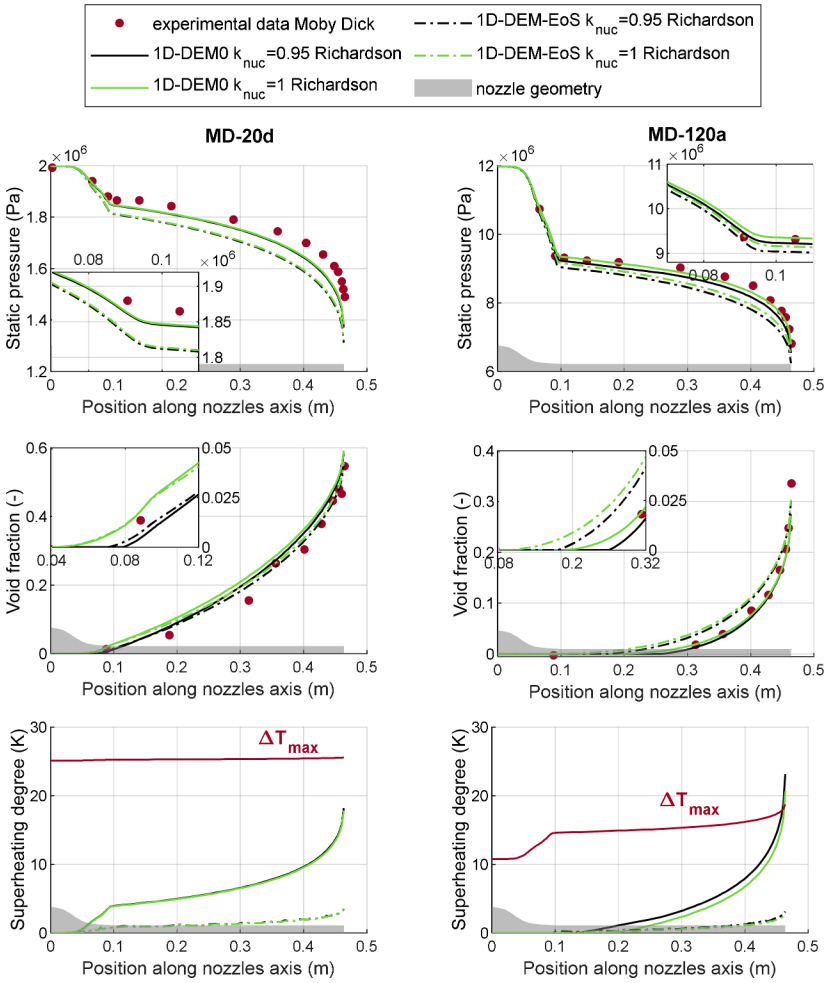

Fig. 14. Effect of different delay in the onset of nucleation (k_{nuc}) and of extrapolating the equation of state into the two-phase region to evaluate the metastable phase properties (DEM-EoS) on the pressure, void fraction and superheating degree profiles for two MD cases.

systematically predicted by Richardson's correlation are due to the higher estimated friction loss with respect to Grönnerud's correlation.

5.3. *Influence of the onset of nucleation and metastable phase properties*

The results obtained applying the proposed novel approach for the metastable phase thermodynamic modelling (DEM-EoS) are presented in this section and the effect of the delay in the onset of nucleation and of the metastable phase thermodynamic properties on the flow prediction is discussed. Water was investigated together with R134a, as the DEM was originally developed for water.

5.3.1. *Water*

The effect of reducing the delay in the onset of vapour nucleation to zero, i.e. imposing $k_{nuc} = 1$ in Eq. (1), and extrapolating the equation of state into the two-phase domain to obtain the metastable liquid thermodynamic properties, on the pressure, void fraction, and degree of superheating profiles is shown in Fig. 14. Reducing the delay in the onset of vapour nucleation has an impact on the solution only locally, at the location where the nucleation starts. On the contrary, the thermodynamic model used for the metastable liquid phase may affect the flow evolution, especially for higher inlet pressures (case MD-120a), where the assumptions of incompressible liquid phase and the linear extrapolation of isotherms into the two-phase domain become less accurate. By looking at the results in Fig. 14, the difference in superheating degree is remarkable in both cases (14.8 K and 20.0 K for the DEM0 with $k_{nuc} = 0.95$ for case MD-20d and MD-120a respectively). The degree of superheating is defined as the difference between the temperature of the metastable liquid phase and the saturation temperature at local pressure. The maximum superheating ΔT_{max} is found at the spinodal point, which is the limit of existence of the metastable phase. With respect to the maximum degree of superheating, the lower pressure case (MD-20d) presents values of superheating degree always within the limit, whereas the superheating degree becomes higher than the maximum value close to the throat for the higher pressure case (MD-120a). This behaviour is unphysical, as it would allow the metastable liquid phase to exist beyond the spinodal line. It is noted however that DEM-EoS underpredicts the pressure profiles compared to the model with incompressible metastable liquid, resulting in a worse agreement with the experimental results. A possible explanation is that the DEM constitutive law was tuned under the assumption of incompressible metastable liquid. A different set of parameters C_1, C_2, and C_3 for the constitutive law in Eq. (2), tailored for DEM-EoS, can arguably increase the accuracy in the pressure prediction to the level of the original DEM. In summary, the decision to use DEM-EoS is driven by its superior physical fidelity in representing the metastable phase, despite a marginal reduction in pressure prediction accuracy.

5.3.2. *R134a*

For R134a, the comparison between different DEM approaches is reported only for case ZE-1, as the other cases present qualitatively the same behaviour. As shown in Fig. 15, the results indicate that using the extrapolation of the equation of state in the two-phase domain for the metastable liquid phase does not give an appreciable difference in

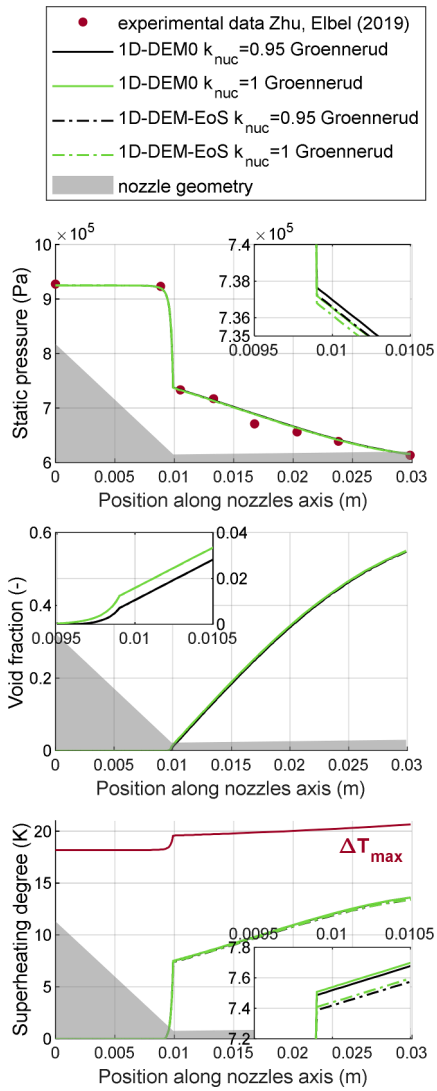

Fig. 15. Effect of different delay in the onset of nucleation (k_{nuc}) and of extrapolating the equation of state into the two-phase region to evaluate the metastable phase properties (DEM-EoS) on the pressure, void fraction and superheating degree profiles for ZE-1 nozzle. The reported uncertainty for pressure measurements is ±0.02 bar.

Table 8
Tuned parameters for DEM correlation for the mass fraction of the mixture in equilibrium with different fixed values of the parameter C_3.

	C_1 (-)	C_2 (-)
DEM0 (C_3=0.22813) Richardson	0.00839	0.63369
DEM-EoS tuned (C_3=0.22813) Grönnerud	0.01086	0.59580
DEM-EoS tuned (C_3=0.25000) Grönnerud	0.01086	0.76482

pressure, void fraction, and superheating degree. As expected, the delay in the onset of nucleation has primarily an influence on the void fraction profile close to where the nucleation starts. In fact, the difference between inlet pressure and pressure at vapour nucleation is around one order of magnitude smaller than in the MD cases presented in Section 5.3.1, so the delay in the onset of nucleation has a marginal effect on the flow. Moreover, the difference in superheating degree between the various approaches is considerably smaller than the one observed for water, as the liquid phase is less compressible for R134a than for water for the considered operating conditions. For the same reason, the superheating degree retained by the metastable liquid phase is higher for R134a than that of water, considering the small inlet-to-throat pressure ratio with respect to MD cases. This is consistent with the lower values of $Ja/\Delta T$ found for R134a in Fig. 3a: a higher ΔT is necessary to have the same Jakob number and, as a consequence, the same volume of metastable liquid predicted by the DEM constitutive law developed for water.

5.4. Tuning of the DEM for R134a

As illustrated in Section 5.2, the original formulation of the DEM combined with the Grönnerud correlation for the Lockhart–Martinelli parameter gives an excellent prediction of the pressure profiles for the ZE nozzles. However, the prediction of the mass flow rate with the same model is less accurate than the one obtained using the Richardson correlation for the Lockhart–Martinelli parameter. Since the constants C_1, C_2 and C_3 in the correlation for the mass fraction of the mixture in equilibrium conditions (Eq. (2)) were originally obtained using Richardson's correlation for friction losses and for water as a working fluid, it is appropriate to obtain a new set of constants for the DEM adopting Grönnerud's correlation for the Lockhart–Martinelli parameter. Hence, in this work a new set of constants was obtained through a gradient-based optimization starting from the original values of the constants reported in Eq. (13). The root mean square relative error calculated on all pressure readings for the cases ZE-1 to ZE-7 was used as objective function. In order to have a single objective for the optimization, the experimental mass flow rate was imposed. In order to avoid stability issues, the constant C_3 was kept fixed during the optimization to the original value ($C_3 = 0.22813$). Moreover, an additional tuning of constants C_1 and C_2 is carried out imposing C_3 to the value $C_3 = 0.25000$, as suggested by Feburie et al.(1993). As already mentioned in Section 2, the constant C_3 is related to the saturation law, which is very similar for water and R134a. The optimized values of the correlation constants after tuning are reported in Table 8.

As the reported relative roughness is higher for the ZE nozzles than the MD nozzles (see k_s/R_2 from Table 2), the optimized value of the constant C_1 related to the nucleation at the wall is increased with respect to the original model (DEM0). The dependence on the roughness levels should be made explicit in the DEM constitutive law, but this would require a large set of experimental data for various roughness levels (Feburie et al., 1993), which is not currently available. The value of the constant C_2 is decreased when $C_3 = 0.22813$ to account for the higher Jakob number of R134a with respect to water, whereas C_2 decreases when $C_3 = 0.25000$ to compensate for the increase in the last term deriving from the higher exponent of the saturation law.

The results in terms of pressure profiles predicted using the DEM-EoS model with original and tuned values of the constants are presented in Fig. 16. The prediction of the pressure profile is improved significantly for case ZE-7, which is an area-dominated case. For all the other cases, which are solutions dominated by the frictional pressure gradient, the prediction of the pressure profile is slightly worse than the one obtained with the original set of constants of the DEM, despite adopting the pressure profile as objective function for the optimization. In fact, the mass flow rate is set to the experimental value during the optimization, allowing to improve the prediction of the mass flow rate with the minimum penalization in terms of pressure profile prediction. As shown in Fig. 17, the estimated mass flow rate is much closer to the experimental data after the tuning of the constants C_1 and C_2, with a reduction of root mean square relative error on the mass flow rate from 10.3 % to 6.1 % when $C_3 = 0.22813$ and 6.8 % when $C_3 = 0.25000$, as reported in Table 9.

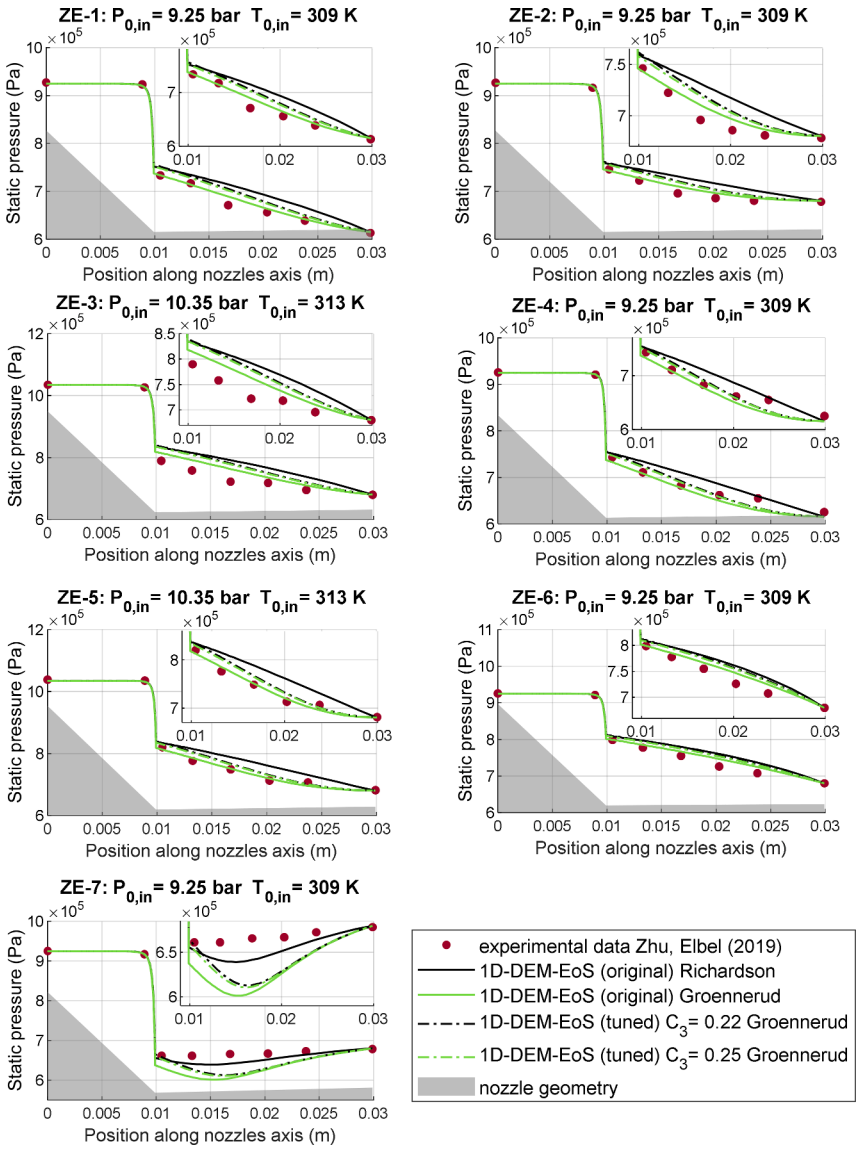

Fig. 16. Comparison between experimental data (Zhu and Elbel, 2019) and results from the 1D-DEM-EoS with original and tuned values of constants C_1 and C_2 and two fixed values of C_3. The reported uncertainty for pressure measurements is ±0.02 bar.

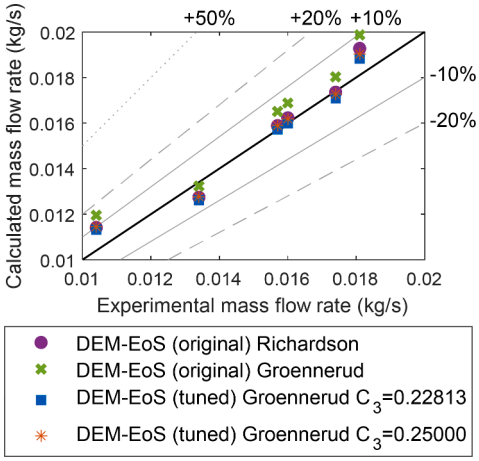

Fig. 17. Comparison between measured (Zhu and Elbel, 2019) and calculated mass flow rate with the 1D-DEM-EoS with original and tuned values of constants C_1 and C_2 and two fixed values of C_3. The reported uncertainty for mass flow rate measurements is $\pm 10^{-4}$ kg/s.

Table 9
Root mean square relative error for mass flow rate calculated with the 1D-DEM-EoS with original and tuned values of constants C_1 and C_2 and two fixed values of C_3.

	DEM-EoS original Richardson	DEM-EoS original Grönnerud	DEM-EoS tuned (C_3 = 0.228127) Grönnerud	DEM-EoS tuned (C_3 = 0.250000) Grönnerud
$e_{m,RMSR}$ (-)	0.069	0.103	0.061	0.068
$\Delta e_{m,RMSR}$ (-)	0.004	0.004	0.004	0.004

6. Conclusions

This paper presents a qualitative characterization of flashing flows of organic fluids and numerical analyses of flashing in converging-diverging nozzles using various 1D models and adopting R134a as reference fluid. First, a state-of-the-art 1D delayed equilibrium model was used to improve the prediction of the flow and then the model was improved by replacing the incompressible flow assumption for the

metastable phase with the computation of the thermodynamic properties through the extrapolation of the equation of state in the two-phase region. In the end, a tuning against experimental data for R134a was performed to obtain a new set of parameters for the constitutive law of the delayed equilibrium model.

As flashing flows are characterized by the presence of high frictional gradients, the adoption of an accurate model for the prediction of viscous losses is crucial and, after a screening of various correlations for the Lockhart–Martinelli parameter, the correlation from Grönnerud was found to be the most suitable for R134a.

By accounting for thermochemical non-equilibrium effects, the original formulation of the delayed equilibrium model was found to improve significantly the prediction of both the mass flow rate and the pressure profile for flashing of R134a with respect to the homogeneous equilibrium model, with a reduction in root mean square relative error on mass flow rate from 48.3 % to 10.3 % and in maximum relative error from 57.3 % to 17.8 %.

The novel formulation of the delayed equilibrium model with the evaluation of the metastable properties through the equation of state was found to predict values of superheating degree below the maximum limit, corresponding to the spinodal point, as opposed to the original formulation. The proposed thermodynamic model for the metastable phase better reflects the physics of the flow, in particular when compressibility effects for the liquid phase are significant.

Tuning the parameter of the delayed equilibrium model correlation against experimental data allowed to account for the differences in thermo-physical properties between organic fluids and water and improved the prediction of the mass flow rate with respect to the original delayed equilibrium model, with a reduction in root mean square relative error from 10.3 % to 6.1 %, while providing an adequate prediction of the pressure profile.

By observing the relevant thermo-physical properties involved in non-equilibrium phenomena in flashing for several organic fluids, it can be concluded that a similar behaviour can be expected for different organic fluids. Therefore, the applicability of the results from this study is not limited to flashing of R134a, but the proposed model can be extended to other organic fluids with a proper adjustment of the delayed equilibrium model correlation to address the differences in saturation law, nozzle geometries and operating conditions.

Since a very limited set of experimental data on flashing of organic fluids in converging-diverging nozzles is available in the literature, further experimental works are crucial to improve the physical understanding of the flashing phenomenon and the accuracy of the proposed model.

CRediT authorship contribution statement

Carlotta Tammone: Conceptualization, Methodology, Software, Validation, Formal analysis, Writing – original draft. **Alessandro Romei:** Conceptualization, Methodology, Formal analysis, Writing – review & editing. **Giacomo Persico:** Conceptualization, Methodology, Formal analysis, Supervision, Writing – review & editing. **Fredrik Haglind:** Conceptualization, Formal analysis, Supervision, Writing – review & editing, Funding acquisition.

Declaration of Competing Interest

The authors declare that they have no known competing financial interests or personal relationships that could have appeared to influence the work reported in this paper.

Data availability

Data will be made available on request.

Appendix A

A.1. Correlations for the Lockhart–Martinelli parameter

The various correlations for the Lockhart–Martinelli parameter used in this work are reported in Table A.1.

Table A.1
Empirical correlations for the Lockhart–Martinelli parameter.

Model	Correlation	
Richardson	$\Phi_{LM}^2 = (1-y)^{-1.75}$	(A.1)
Grönnerud	$\Phi_{LM}^2 = 1 + \left(\frac{dp}{dz}\right)_{Fr} \cdot \left[\frac{\rho_L/\rho_V}{(\mu_L/\mu_V)^{0.25}} - 1\right]$	(A.2)
	$\left(\frac{dp}{dz}\right)_{Fr} = f_{FR} \cdot [x + 4 \cdot (x^{1.8} - x^{10} f_{FR}^{0.5})]$	
	$\begin{cases} f_{FR} = Fr_L^{0.3} + 0.0055 \cdot [\ln(1/Fr_L)]^2 \text{ if } Fr_L < 1 \\ f_{FR} = 1 \text{ if } Fr_L \geq 1 \end{cases}$	
	$Fr_L = \frac{G_L^2}{gD\rho_L}$	
Friedel	$\Phi_{LM}^2 = E + \frac{3.24 \cdot F \cdot H}{Fr_h^{0.045} \cdot We_L^{0.035}}$	(A.3)
	$E = (1-x)^2 + x^2 \frac{\rho_L \cdot f_V}{\rho_V \cdot f_L}$	
	$F = x^{0.78} \cdot (1-x)^{0.224}$	
	$H = \left(\frac{\rho_L}{\rho_V}\right)^{0.91} \left(\frac{\mu_V}{\mu_L}\right)^{0.19} \left(1 - \frac{\mu_V}{\mu_L}\right)^{0.7}$	
	$We_L = \frac{GD}{\sigma\rho_h}$	
	$\rho_h = \left(\frac{x}{\rho_V} + \frac{1-x}{\rho_L}\right)^{-1}$	

(continued on next page)

Table A.1 (*continued*)

Model	Correlation
Beattie	$\begin{cases} \Phi_{LM}^2 = \left[1+x\left(\frac{\rho_L}{\rho_V}-1\right)\right]^{0.8}\cdot\left\{1+x\left[\frac{(3.5\mu_V+2\mu_L)\rho_L}{(\mu_V+\mu_L)\rho_V}-1\right]\right\}^{0.2} & if\ y<0.3 \\ \Phi_{LM}^2 = \left[1+x\left(\frac{\rho_L}{\rho_V}-1\right)\right]^{0.8}\cdot\left[1+x\left(3.5\frac{\rho_L}{\rho_V}-1\right)\right]^{0.2} & if\ 0.3\le y\le 0.8 \\ \Phi_{LM}^2 = \left[1+x\left(\frac{\rho_L}{\rho_V}-1\right)\right]^{0.8}\cdot\left[1+x\left(\frac{\mu_V\rho_L}{\mu_L\rho_V}-1\right)\right]^{0.2} & if\ 0.8\le y\le 0.95 \\ \Phi_{LM}^2 = \left(\frac{\mu_V}{\mu_L}\right)^{0.2}\left(\frac{\rho_V}{\rho_L}\right)^{0.8}\left[1+x\left(\frac{\rho_L}{\rho_v}-1\right)\right]^{1.8} & if\ y>0.95 \end{cases}$ (A.4)
Chisholm	$\Phi_{LM}^2 = 1+(Y^2-1)\cdot\left[Bx^{\frac{2-n}{n}}\cdot(1-x)^{\frac{(2-n)}{n}}\cdot x^{2-n}\right]$ (A.5) $\begin{cases} n=1\ if\ Re<2000 \\ n=0.25\ if\ Re\ge 2000 \end{cases}$ $Y^2 = \left(\frac{dp}{dz}\right)_{fr,V}/\left(\frac{dp}{dz}\right)_{fr,L}$ If $0<Y<9.5$: $\begin{cases} B=55/G^{0.5}\ G\ge 1900\ kg/m^2s \\ B=2400/G\ 5000<G<1900\ kg/m^2s \\ B=4.8\ G\le 500\ kg/m^2s \end{cases}$ If $9.5\le Y\le 28$: $\begin{cases} B=\frac{520}{Y\cdot G^{0.5}}\ G\le 600\ kg/m^2s \\ B=21/Y\ G>600\ kg/m^2s \end{cases}$ If $Y>28$: $B=\frac{15000}{Y^2\cdot G^{0.5}}$

A.2. Grid convergence study

A grid convergence study was performed in order to choose the number of control volumes of the grid. For ZE cases and NA cases an optimal number of nodes was found to be 100. For the MD cases the optimal number of nodes was found to be 150. The results from the grid convergence study for the cases reported in Table A.2 are shown in Figs. A.1, A2, A3, A4, A5, A6 and A.7, where the difference between the adopted grids is quantified in terms of the relative difference in pressure at the throat ($\Delta P_{th,rel}$), in pressure at the outlet ($\Delta P_{out,rel}$), and in mass flow rate (Δm_{rel}). The relative difference is computed with respect to the value with the maximum number of nodes (the finest grid solution):

$$\Delta X_{rel} = \frac{X_N - X_{N_{max}}}{X_{N_{max}}} \tag{A.6}$$

Where X is the considered quantity and N is the number of nodes of the grid and N_{max} is the maximum number of grid nodes.

The cases reported here have been selected because they are the solutions where the highest gradients in thermodynamic properties along the nozzle axis have been found and they are therefore the cases where the highest difference between grids with different number of nodes was found. When the solution was obtained imposing the pressure at the outlet, as in cases ZE-1 and ZE-7 using the DEM-EoS (Figs. A.4 and A.7), the relative difference in pressure at the outlet is not relevant because this value is imposed during the solution procedure.

Table A.2
Cases and models for which the grid convergence study was performed.

Case	Model	Type of flow	Figure
NA-9d	HEM Friedel	Choked supersonic	Fig. A.1
MD-20d	DEM0 Richardson	Choked supersonic	Fig. A.2
MD-120b	DEM0 Richardson	Choked supersonic	Fig. A.3
ZE-1	HEM Grönnerud	Choked supersonic	Fig. A.4
ZE-1	DEM-EoS Grönnerud	Subsonic Imposed P_{out}	Fig. A.5
ZE-7	HEM Grönnerud	Choked supersonic	Fig. A.6
ZE-7	DEM-EoS Grönnerud	Subsonic Imposed P_{out}	Fig. A.7

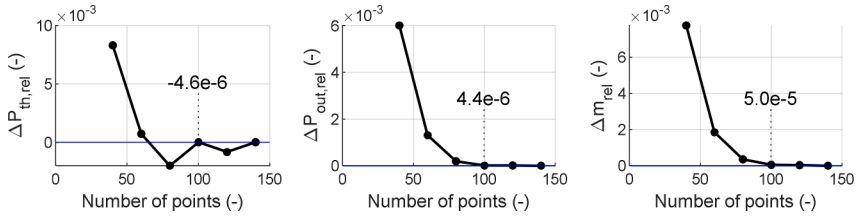

Fig. A.1. Grid convergence study for case NA-9d using HEM and Friedel correlation for the Lockhart–Martinelli parameter.

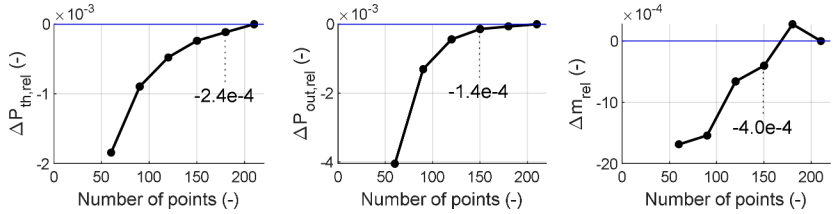

Fig. A.2. Grid convergence study for case MD-20d using DEM0 and Richardson correlation for the Lockhart–Martinelli parameter.

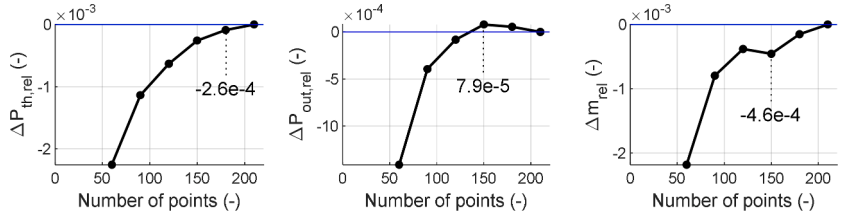

Fig. A.3. Grid convergence study for case MD-120b using DEM0 and Richardson correlation for the Lockhart–Martinelli parameter.

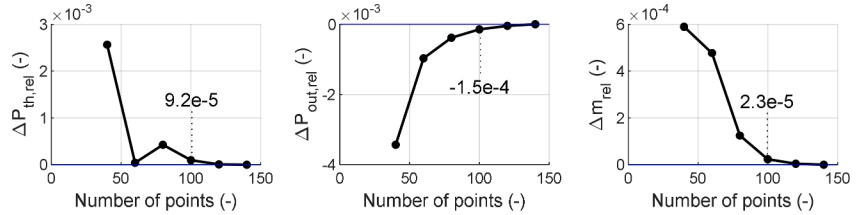

Fig. A.4. Grid convergence study for case ZE-1 using HEM and Grönnerud correlation for the Lockhart–Martinelli parameter.

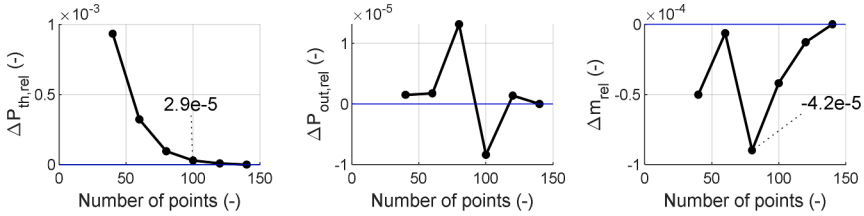

Fig. A.5. Grid convergence study for case ZE-1 using DEM-EoS and Grönnerud correlation for the Lockhart–Martinelli parameter.

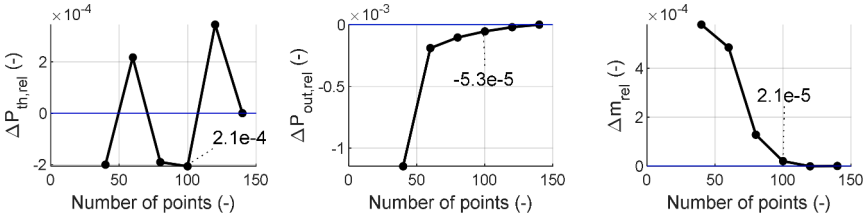

Fig. A.6. Grid convergence study for case ZE-7 using HEM and Grönnerud correlation for the Lockhart–Martinelli parameter.

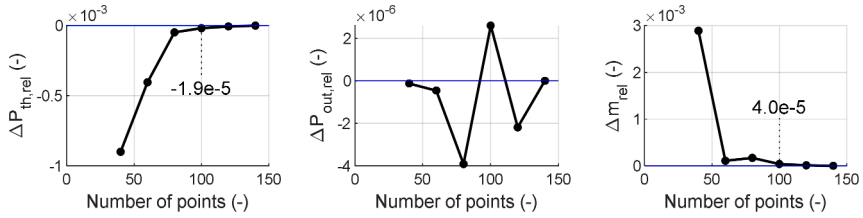

Fig. A.7. Grid convergence study for case ZE-7 using DEM-EoS and Grönnerud correlation for the Lockhart–Martinelli parameter.

References

Angielczyk, W., Bartosiewicz, Y., Butrymowicz, D., 2020. Development of delayed equilibrium model for CO2 convergent-divergent nozzle transonic flashing flow. Int. J. Multiph. Flow 131, 103351. https://doi.org/10.1016/j.ijmultiphaseflow.2020.103351.

Angielczyk, W., Seynhaeve, J., Butrymowicz, D., Bartosiewicz, Y., 2010. 1-D modeling of supersonic carbon dioxide two-phase flow through ejector motive nozzle. Int. Refrig. Air Cond. Conf. Purdue 1–8.

Angielczyk, W., Seynhaeve, J.M., Gagan, J., Bartosiewicz, Y., Butrymowicz, D., 2019. Prediction of critical mass rate of flashing carbon dioxide flow in convergent-divergent nozzle. Chem. Eng. Process. - Process Intensif. 143, 107599 https://doi.org/10.1016/J.CEP.2019.107599.

Bartosiewicz, Y., Seynhaeve, J.M., 2013. Delayed equilibrium model (DEM) of flashing choked flows relevant to LOCA. Multiph. Sci. Technol. 25, 117–131. https://doi.org/10.1615/MULTSCIENTECHN.V25.I2-4.50.

Beattie, D.R.H., 1973. A note on the calculation of two-phase pressure losses. Nucl. Eng. Des. 25, 395–402.

Bell, I.H., Wronski, J., Quoilin, S., Lemort, V., 2014. Pure and pseudo-pure fluid thermophysical property evaluation and the open-source thermophysical property library coolprop. Ind. Eng. Chem. Res. 53, 2498–2508. https://doi.org/10.1021/IE4033999/SUPPL_FILE/IE4033999_SI_002.ZIP.

Bilicki, Z., Kestin, J., 1990. Physical aspects of the relaxation model in two-phase flow. Proc. R. Soc. London. A. Math. Phys. Sci. 428, 379–397. https://doi.org/10.1098/rspa.1990.0040.

Bouré, J.A., Fritte, A.A., Giot, M.M., Réocreux, M.L., 1976. Highlights of two-phase critical flow: on the links between maximum flow rates, sonic velocities, propagation and transfer phenomena in single and two-phase flows. Int. J. Multiph. Flow 3, 1–22. https://doi.org/10.1016/0301-9322(76)90030-6.

Brennen, C.E., 2005. Fundamentals of Multiphase Flow, Fundamentals of Multiphase Flow. Cambridge University Press. https://doi.org/10.1017/CBO9780511807169.

Chisholm, D., 1973. Pressure gradients due to friction during the flow of evaporating two-phase mixtures in smooth tubes and channels. Int. J. Heat Mass Transf. 16, 347–358. https://doi.org/10.1016/0017-9310(73)90063-X.

Clamond, D., 2009. Efficient resolution of the colebrook equation. Ind. Eng. Chem. Res. 48, 3665–3671. https://doi.org/10.1021/IE801626G/ASSET/IMAGES/MEDIUM/IE-2008-01626G_0005.GIF.

De Lorenzo, M., Lafon, P., Pelanti, M., Pantano, A., Di Matteo, M., Bartosiewicz, Y., Seynhaeve, J.M., 2021. A hyperbolic phase-transition model coupled to tabulated EoS for two-phase flows in fast depressurizations. Nucl. Eng. Des. 371, 110954 https://doi.org/10.1016/J.NUCENGDES.2020.110954.

De Lorenzo, M., Lafon, P., Seynhaeve, J.-M., Bartosiewicz, Y., 2017. Benchmark of delayed equilibrium model (DEM) and classic two-phase critical flow models against experimental data. Int. J. Multiph. Flow 92, 112–130. https://doi.org/10.1016/j.ijmultiphaseflow.2017.03.004.

Downar-Zapolski, P., Bilicki, Z., Bolle, L., Franco, J., 1996. The non-equilibrium relaxation model for one-dimensional flashing liquid flow. Int. J. Multiph. Flow 22, 473–483. https://doi.org/10.1016/0301-9322(95)00078-X.

Feburie, V., Giot, M., Granger, S., Seynhaeve, J., Murakoshi, I., Ikegami, F., 1993. A model for choked flow through cracks with inlet subcooling. Int. J. Multiph. Flow 19, 541–562. https://doi.org/10.1016/0301-9322(93)90087-B.

Friedel, L., 1979. Improved friction pressure drop correlation for horizontal and vertical two-phase pipe flow. In: Proc. of European Two-Phase Flow Group Meet.

Giacomelli, F., Mazzelli, F., Milazzo, A., 2018. A novel CFD approach for the computation of R744 flashing nozzles in compressible and metastable conditions. Energy 162, 1092–1105. https://doi.org/10.1016/j.energy.2018.08.050.

Grönnerud, R., 1972. Investigation of liquid hold-up, flow resistance and heat transfer in circulation type evaporators, part IV: two-phase flow resistance in boiling refrigerants. Bull. l'Inst. Du Froid Annex 1, 127–138.

Ishii, M., Hibiki, T., 2006. Thermo-Fluid Dynamics of Two-Phase Flow. Springer US, Boston, MA. https://doi.org/10.1007/978-0-387-29187-1.

Lackme, C., 1979. Incompleteness of the flashing of a supersaturated liquid and sonic ejection of the produced phases. Int. J. Multiph. Flow 5, 131–141. https://doi.org/10.1016/0301-9322(79)90041-7.

Lee, J.S., Kim, Min Soo, Kim, Mo Se, 2011. Experimental study on the improvement of CO2 air conditioning system performance using an ejector. Int. J. Refrig. 34, 1614–1625. https://doi.org/10.1016/J.IJREFRIG.2010.07.025.

Lettieri, C., Yang, D., Spakovszky, Z., 2015. An investigation of condensation effects in supercritical carbon dioxide compressors. J. Eng. Gas Turbines Power 137. https://doi.org/10.1115/1.4029577/373524.

Liao, Y., Lucas, D., 2021. A review on numerical modelling of flashing flow with application to nuclear safety analysis. Appl. Therm. Eng. 182, 116002 https://doi.org/10.1016/J.APPLTHERMALENG.2020.116002.

Liao, Y., Lucas, D., 2017. Computational modelling of flash boiling flows: a literature survey. Int. J. Heat Mass Transf. 111, 246–265. https://doi.org/10.1016/J.IJHEATMASSTRANSFER.2017.03.121.

Lund, H., Flåtten, T., 2010. Equilibrium conditions and sound velocities in two-phase flows. In: Proceedings of the SIAM Annual Meeting.

MATLAB R2022a, 2022.

Nakagawa, M., Berana, M.S., Kishine, A., 2009. Supersonic two-phase flow of CO2 through converging–diverging nozzles for the ejector refrigeration cycle. Int. J. Refrig. 32, 1195–1202. https://doi.org/10.1016/j.ijrefrig.2009.01.015.

Nguyen, D.L., Winter, E.R.F., Greiner, M., 1981. Sonic velocity in two-phase systems. Int. J. Multiph. Flow 7, 311–320. https://doi.org/10.1016/0301-9322(81)90024-0.

Ould Didi, M.B., Kattan, N., Thome, J.R., 2002. Prediction of two-phase pressure gradients of refrigerants in horizontal tubes. Int. J. Refrig. 25, 935–947. https://doi.org/10.1016/S0140-7007(01)00099-8.

Palacz, M., Smolka, J., Fic, A., Bulinski, Z., Nowak, A.J., Banasiak, K., Hafner, A., 2015. Application range of the HEM approach for CO2 expansion inside two-phase ejectors for supermarket refrigeration systems. Int. J. Refrig. 59, 251–258. https://doi.org/10.1016/j.ijrefrig.2015.07.006.

Persico, G., Gaetani, P., Romei, A., Toni, L., Bellobuono, E.F., Valente, R., 2021. Implications of phase change on the aerodynamics of centrifugal compressors for supercritical carbon dioxide applications. J. Eng. Gas Turbines Power 143, 1–11. https://doi.org/10.1115/1.4049924.

Pinhasi, G.A., Ullmann, A., Dayan, A., 2005. Modeling of flashing two-phase flow. Rev. Chem. Eng. 21, 133–264. https://doi.org/10.1515/REVCE.2005.21.3-4.133.

Richardson, B.L.L., 1958. Some problems in horizontal two-phase tow-component flow. Argonne, IL (United States). 10.2172/4304321.

Ringstad, K.E., Allouche, Y., Gullo, P., Ervik, Å., Banasiak, K., Hafner, A., 2020. A detailed review on CO2 two-phase ejector flow modeling. Therm. Sci. Eng. Prog. 20, 100647 https://doi.org/10.1016/j.tsep.2020.100647.

Romei, A., Persico, G., 2021. Computational fluid-dynamic modelling of two-phase compressible flows of carbon dioxide in supercritical conditions. Appl. Therm. Eng. 190, 116816 https://doi.org/10.1016/j.applthermaleng.2021.116816.

Rony, R.U., Yang, H., Krishnan, S., Song, J., 2019. Recent advances in transcritical CO 2 (R744) heat pump system: a review. Energies 12. https://doi.org/10.3390/EN12030457.

Simões-Moreira, J., Bullard, C., 2003. Pressure drop and flashing mechanisms in refrigerant expansion devices. Int. J. Refrig. 26, 840–848. https://doi.org/10.1016/S0140-7007(03)00070-7.

Smith, I.K., da Silva, R.P.M., 1994. Development of the trilateral flash cycle system part 2: increasing power output with working fluid mixtures. Proc. Inst. Mech. Eng. Part A J. Power Energy 208, 135–144. https://doi.org/10.1243/PIME_PROC_1994_208_022_02.

Sumeru, K., Nasution, H., Ani, F.N., 2012. A review on two-phase ejector as an expansion device in vapor compression refrigeration cycle. Renew. Sustain. Energy Rev. 16, 4927–4937. https://doi.org/10.1016/j.rser.2012.04.058.

Tammone, C., Pili, R., Indrehus, S., Haglind, F., 2021. Techno-economic analysis of partial evaporation organic Rankine cycle systems for geothermal applications. 6 th Int. Semin. ORC Power Syst. https://doi.org/10.14459/2021MP1633026.

Tammone, C., Romei, A., Persico, G., Haglind, F., 2023. Non-equilibrium phenomena in two-phase flashing flows of organic fluids. 4th International Seminar on Non-Ideal Compressible Fluid Dynamics (NICFD2022). Springer, pp. 135–145.

Tentner, A., Weisman, J., 1978. The use of the method of characteristics for examination of two-phase flow behavior. Nucl. Technol. 37, 19–28. https://doi.org/10.13182/NT78-A32087.

van Heule, X., Skiadopoulos, A., Manolakos, D., De Paepe, M., Lecompte, S., 2023. Modelling of two-phase expansion in a reciprocating expander. Appl. Therm. Eng. 218, 119224 https://doi.org/10.1016/J.APPLTHERMALENG.2022.119224.

White, M.T., 2022. Investigating the wet-to-dry expansion of organic fluids for power generation. Int. J. Heat Mass Transf. 192, 122921 https://doi.org/10.1016/j.ijheatmasstransfer.2022.122921.

White, M.T., 2021. Cycle and turbine optimisation for an ORC operating with two-phase expansion. Appl. Therm. Eng. 192, 116852 https://doi.org/10.1016/j.applthermaleng.2021.116852.

Zhu, J., Elbel, S., 2020. CFD simulation of vortex flashing R134a flow expanded through convergent-divergent nozzles. Int. J. Refrig. 112, 56–68. https://doi.org/10.1016/j.ijrefrig.2019.12.005.

Zhu, J., Elbel, S., 2019. Measurement of static pressure profiles of vortex flashing R134a flow expanded through convergent–divergent nozzles. Int. J. Refrig. 108, 258–270. https://doi.org/10.1016/j.ijrefrig.2019.08.023.